International Journal of
Molecular Sciences

MDPI

Article

Pyrrolocytosine as a Fluorescent Sensor of RNA–Small Molecule Interactions

Taylor L. Coulson [1], Gavin A. Valdez [1] and Julia R. Widom [1,2,*]

[1] Department of Chemistry and Biochemistry, University of Oregon, Eugene, OR 97403, USA; tcoulson@uoregon.edu (T.L.C.); gvaldez@uoregon.edu (G.A.V.)
[2] Oregon Center for Optical, Molecular and Quantum Science, University of Oregon, Eugene, OR 97403, USA
* Correspondence: jwidom@uoregon.edu

Abstract

Fluorescent base analogues have proven to be valuable probes of RNA structure. Pyrrolocytosine (pC), an analogue of cytosine, exhibits highly environment-sensitive fluorescence within RNA and is strongly quenched in hydrogen-bonded contexts. In this work, we incorporated pC into the aptamer domain of the *B. subtilis* guanine riboswitch to determine if this quenching mechanism could allow for sensing of RNA–small molecule interactions. We utilized complementary fluorescence spectroscopy methods to understand the functional impacts and ligand sensitivity of pC substitutions distal to and within the binding pocket. We found that pC substitution within a static structural region exhibits the expected ligand-independent fluorescence properties. When placed in the ligand binding pocket, pC exhibits a moderately decreased affinity for the ligands guanine (G) and hypoxanthine (Hx) while maintaining high specificity for G. We found that pC behaves as a turn-off sensor, with distinct changes in fluorescence upon G or Hx binding. These differences are dependent on the number of hydrogen bonds formed with pC and are resolvable in both time-dependent and steady-state fluorescence measurements. Our results show that pC can be used to study RNA–small molecule interactions and can discriminate between similar ligands even when they have identical binding modes.

Keywords: spectroscopy; circular dichroism; TCSPC; fluorescence lifetimes; base analogue; riboswitch; RNA; binding specificity; kinetics

1. Introduction

Decades of RNA research have expanded our understanding of its biological roles from a simple carrier of genetic information to a molecule with wide-ranging regulatory capacity. Regulatory functions are commonly achieved by non-coding RNAs (ncRNAs), which are transcribed from regions of the genome that do not encode protein, as well as non-coding domains of messenger RNAs (mRNAs) termed "untranslated regions" (UTRs). These transcripts and motifs have been shown to be required for the regulation of gene expression in bacteria [1] and their dysregulation has been identified in multiple disease states [2]. As a result, ncRNAs and motifs found in UTRs have seen increased research interest for their potential as therapeutic targets [3–6]. Riboswitches, which are found primarily in the 5′ UTRs of bacterial mRNAs, represent one class of RNA motifs that has garnered such interest. Riboswitches control expression of downstream genes in response to environmental stimuli, typically at the transcriptional or translational level. These molecular switches consist of two domains, the aptamer domain and the expression platform. The aptamer domain

Check for updates

Academic Editor: Qinglong Qiao

Received: 29 September 2026
Revised: 21 October 2026
Accepted: 26 October 2026
Published: 28 October 2026

Copyright: © 2026 by the authors. Licensee MDPI, Basel, Switzerland. This article is an open access article distributed under the terms and conditions of the Creative Commons Attribution (CC BY) license.

binds ligands in the cellular environment and undergoes a conformational change upon binding; this induces a further structural change in the expression platform through a switching sequence that links the two domains, resulting in ligand-dependent regulation of the downstream genes [7,8]. Structure-guided modification of native riboswitch ligands has been shown to be a promising avenue of initial drug candidate design [9,10], and novel synthetic ligands targeting riboswitches have shown regulatory effects in different bacterial strains [11–13]. A more thorough understanding of how ligand binding is coupled to the local conformation within the aptamer domain can aid in the design of novel ligands that may have potential as drug candidates.

Fluorescence-based methods are widely used to investigate RNA's structure in solution and how it changes in response to environmental stimuli, though this approach requires labeling with a minimally perturbing probe that is sensitive to the RNA's structure [14–17]. For example, fluorescent base analogues (FBAs) are structural mimics of native nucleic acid bases with increased fluorescence quantum yields and can be incorporated into an RNA at a location of interest [18,19]. FBAs are typically designed to maintain the base pairing of their corresponding native bases, though the structural modifications implemented for improved fluorescence have the potential to perturb the RNA tertiary structure [20]. Many FBAs exhibit environment-sensitive fluorescence [21–24], making them useful probes of local nucleic acid structure, and new FBAs with distinct photophysical and structural properties are constantly being developed [25–28].

Pyrrolocytosine (pC; Figure 1A) was first utilized as a deoxycytidine analogue to investigate the formation of the RNA:DNA hybrid in the transcription bubble [29]. More recent investigations have utilized pC to investigate the folding of a ribozyme [30] and intermolecular interactions between tRNA and the T-Box riboswitch [31]. Previous experimental and computational studies showed that within DNA oligonucleotides, pC exhibits fluorescence enhancement in base-stacked conformations while hydrogen bonding quenches its fluorescence [32,33]. Building on this work, we recently showed that while the established photophysical impacts of base stacking and hydrogen bonding persist in RNA, there is also a strong sequence dependence not previously reported in DNA. Additionally, we showed that the base-paired state of pC within a duplex can be resolved using fluorescence lifetime measurements as a highly populated, rapidly decaying time component, and that the lineshape of its emission spectrum is a reporter of local polarity [34]. These results supported the notion that pC could act as a multifaceted probe of local structure when utilized in more complex RNA species.

Most studies that utilize FBAs, including pC, do so by labeling sites that undergo environment-sensitive reorganization of stacking or base-pairing interactions [30,31,35]. A yet unexplored application of pC's unique fluorescence properties is the investigation of small molecule interactions with RNA. While the widely used 2-aminopurine (2-AP) has been used to understand the ligand-dependent conformational changes of riboswitches, it has typically been placed in distal regions of the aptamer domain that do not directly interact with the ligand [36–39] or in rarer cases has been used as a ligand analogue [40–42]. While 2-AP and many other FBAs are quenched primarily through base stacking [43,44], pC's hydrogen bond-dependent quenching presents the opportunity for its application as a direct turn-off sensor of ligand binding in riboswitches that rely on hydrogen bonds between the ligand and a cytosine residue (Figure 1B). The guanine riboswitch (GR; Figure 1C,D) aptamer domain coordinates guanine (G) and its metabolic derivatives with varying affinity through a Watson–Crick–Franklin (WCF) hydrogen bonding pattern to a conserved cytosine base, C74 (Figure 1E) [41,45]. This riboswitch acts through a hybrid conformational selection/induced fit model [41]; its three-way junction is largely pre-organized while an unhybridized linker (J2/3, Figure 1C) between two adjacent stem-loops samples "open"

and "closed" conformations, where only the open conformation is capable of binding to a ligand [46,47]. We hypothesized that pC substituted for C74 could act as a conformationally sensitive reporter of ligand binding, while pC substituted elsewhere could reveal whether ligand binding is coupled to conformational changes distal to the binding pocket.

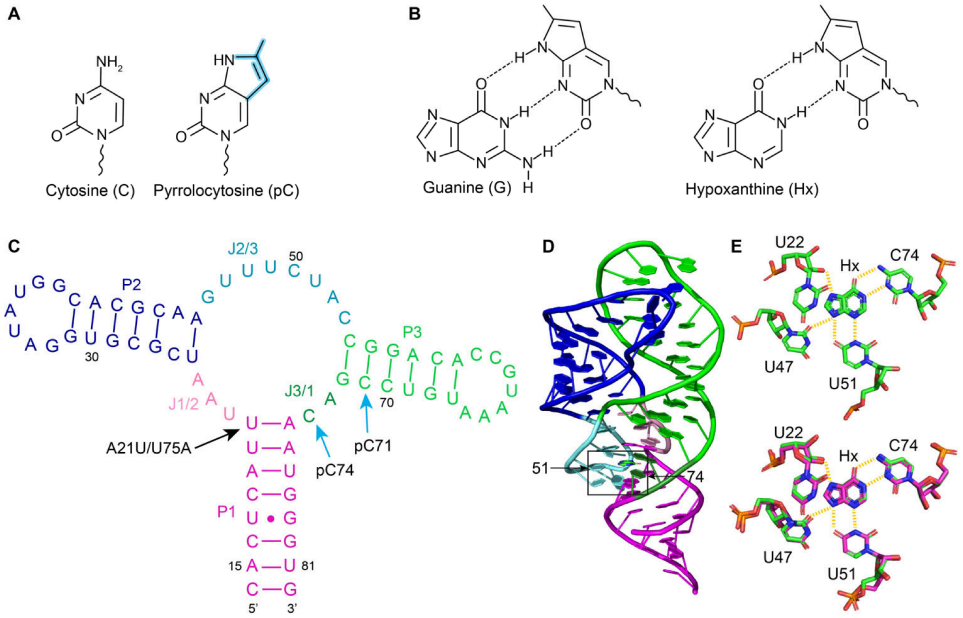


Figure 1. Pyrrolocytosine and the guanine riboswitch. (**A**) Chemical structures of cytosine (left) and pyrrolocytosine (pC; right). Modifications are highlighted in blue on the pC structure. (**B**) Hydrogen bonding patterns between pC and guanine (left) or hypoxanthine (right). (**C**) The sequence and secondary structure of the A21U/U75A mutant of the *B. subtilis* GR utilized in this study. Mutations and sites of pC labeling are indicated with arrows. (**D**) The crystal structure of the Hx-bound A21U/U75A mutant of the *B. subtilis* GR (PDB ID 2EES) with domains color-coded as in panel (**C**). (**E**) Top: A close-up of the binding pocket (box in panel (**D**)) showing hydrogen bonds between Hx and nearby bases. Bottom: An overlay of binding pocket structures of WT (PDB ID 4FE5) and A21U/U75A (PDB ID 2EES) GR variants. Structures are color-coded by atom, where C is green (2EES) or pink (4FE5).

In this work, we utilized both steady-state and time-dependent spectroscopic methods to monitor pC's fluorescence properties within GR in response to the binding of ligands with varying affinities and degrees of hydrogen bonding (Figure 1B). pC substituted within the P3 helix confirmed that this domain is base-paired both with and without ligand, while pC substituted for C74 exhibited ligand-dependent quenching while maintaining specificity, as assessed through both equilibrium binding affinity and binding kinetics. The emission lineshape of pC indicated different levels of solvent accessibility at these two labeling sites, and both sites showed evidence of conformational heterogeneity both with and without ligand. These results demonstrate that pC can be a valuable tool for measuring the conformational states accessible to riboswitches using both steady-state and time-dependent methods.

2. Results and Discussion

2.1. Design of pC-Based GR Sensors

The GR was selected as a model system for this study as its ligand specificity is conferred by a key cytosine residue [41,48] (C74) and it has longstanding interest as a pharmaceutical target [10–13,49]. Specifically, the *Bacillus subtilis* GR aptamer domain has been the subject of extensive biochemical and structural characterization [41,45,47,50–54], allowing

for informed labeling site selection and guiding interpretation of experimental results. We selected two pC labeling sites within a 69-nucleotide sequence encompassing the *B. subtilis* GR aptamer domain: positions 71 and 74 (Table 1). Position 71 resides within P3 (Figure 1C) and remains base-paired independently of Mg^{2+} and ligand [52]. pC71 is therefore expected to remain in a highly quenched state, defined by a low emission intensity and short fluorescence lifetime, and observations to the contrary would be indicative of pC altering the surrounding structure.

Table 1. The sequences of oligonucleotides used in this study. A vertical line indicates the site at which two oligonucleotides were ligated together to form the full-length GR.

	Sequence
Unmodified GR	5′ CAC UCA UUU AAU CGC GUG GAU AUG GCA CGC AAG UUU CUA CCG GGC ACC GUA AAU GU|C CGA CAA UGG GUG
pC71 GR	5′ CAC UCA UUU AAU CGC GUG GAU AUG GCA CGC AAG UUU CUA CCG GGC ACC GUA AAU GU|C (pC)GA CAA UGG GUG
pC74 GR	5′ CAC UCA UUU AAU CGC GUG GAU AUG GCA CGC AAG UUU CUA CCG GGC ACC GUA AAU GU|C CGA (pC)AA UGG GUG
DNA Splint	5′ CAC CCA TTG TCG GAC ATT TAC GGT GCC CG
Strand 1 ApCA	5′ AUA AUU CCA (pC)AC CUU AUA UUA
Strand 2 UGU	5′ UAA UAU AAG GUG UGG AAU UAU
Strand 2 UIU	5′ UAA UAU AAG GUI UGG AAU UAU
Strand 2 UUU	5′ UAA UAU AAG GUU UGG AAU UAU

The binding affinity and specificity of GR is determined primarily by the extent of hydrogen bonding between a potential ligand and C74 [41,45,48]. pC74 is therefore expected to experience strong fluorescence quenching in the presence of ligand, as we have previously demonstrated that base pairing of pC with G results in reduced emission intensity and a dominant fast decay component [34]. In order to test whether pC74 GR maintained the ligand binding properties of the native GR and to investigate the dependence of pC fluorescence on the number of hydrogen bonds formed, we carried out all measurements with both G, which forms three hydrogen bonds with C, and a lower affinity ligand, hypoxanthine (Hx), which lacks a C2 primary amine and therefore only forms two hydrogen bonds with C74 (Figure 1B).

To optimize this sensor, the sequence context of pC also had to be considered. We previously demonstrated that pC's fluorescence within RNA is strongly sequence-dependent, with adjacent A and C residues conferring the greatest fluorescence enhancement over free pC riboside. Adjacent U residues confer the weakest enhancement and yield three-component fluorescence decays, leading to a more complex structural interpretation than required in other sequence contexts [34]. In the selected *B. subtilis* GR, C74 resides between A73 and U75, the latter of which makes a base pair with A21. Based on our previous results showing divergent properties of pC when adjacent to A and U, we asked whether the sequence might offer any flexibility that could be exploited to improve performance. Interestingly, nucleotides 21 and 75 have been shown to covary across species to maintain the A-U WCF base pair (A21/U75 in 90% of species and U21/A75 in 10%) [55], and mutational studies have shown that affinity for G is identical in WT and A21U/U75A, and is impaired only slightly in A21G/U75C [53,56]. The affinity for Hx is affected, with a K_D of 0.76 μM for WT GR and 3.3 μM for A21U/U75A at 30 °C in 10 mM Mg^{2+} [56]. However, X-ray crystallography of GR bound to Hx has shown that its structure is unchanged by the A21U/U75A transversion, including the hydrogen bonding network around the ligand (Figure 1E), and the adjacent "platform" created by the 21–75 base pair and C50 [53]. We therefore hypothesized that a pC-labeled A21U/U75A mutant could act as a functional sensor.

A common quenching mechanism for FBAs is the formation of low-energy charge transfer (CT) states [57–61]; so, we performed quantum mechanical (QM) calculations to ask whether they were likely to be present in any of the sequence contexts under consideration. QM calculations performed on the A-form trimers ApCA, UpCU and ApCU all showed an absence of low-energy CT states, with S0-S1 being a strong π-π* transition localized on pC (Figure S1), similar to our previous observations with CpCC and GpCG. The S2 state was at least 0.6 eV higher in energy in all cases. The same observations held when QM calculations were performed on ApCA and ApCU trimers in the geometry of the GR binding pocket observed crystallographically (PDB: 4FE5 [45], 2EES [53]; Figure S1). While these results did not reveal an obvious photophysical justification for any particular sequence, it remained advantageous to obtain maximal pC fluorescence intensity and more readily interpretable results by removing sequence-dependent variables where possible. We therefore placed pC74 in the more favorable ApCA context by introducing the compensatory mutation A21U/U75A (Figure 1C), taking advantage of the biochemical and structural characterization discussed above.

2.2. pC71 Exhibits Stable Base Pairing

We first consider pC71, which replaces a base-paired C residue within the P3 helix (Figure 1C). This helix is intact in the isolated RNA [52], so we anticipated a low emission intensity and little change in the fluorescence properties upon addition of Mg^{2+} or ligand. Indeed, the emission and excitation spectra of pC71 GR show no change in intensity or lineshape upon addition of 1 mM Mg^{2+}, and only a small decrease in intensity upon addition of saturating G or Hx (4 μM or 310 μM, respectively) (Figure 2A,B). The initial low emission intensity suggests that pC71 is in a base-paired state, and the observed decrease upon addition of G/Hx could be attributed to increased base-pairing stability within P3. As C71 does not directly interact with the bound ligand, this consistent response indicates that pC71 does not disrupt the global structure of the riboswitch. Of particular note is the distinct emission lineshape that pC71 GR exhibits relative to previously reported pC-labeled RNAs. While the suppressed "red shoulder" associated with highly stacked and solvent shielded environments [34] is clearly visible at ~470 nm, there is an additional longer wavelength (~530 nm) feature indicating a distinct solvation environment within this highly ordered region of GR (Figures 2A and S2A).

The hydrogen-bonded state of pC71 is further confirmed by time-correlated single photon counting (TCSPC; Figure 2C,D). In these measurements, all emission at wavelengths longer than 420 nm was collected (see Section 3.3.2); thus, all spectral features discussed above are represented in the resulting data. pC71 fluorescence decays were well fit ($\chi^2 = 1.10$) with a model consisting of a slow exponential decay component and a shorter component described by a gamma distribution [62], termed a "1E1G_S" model (details in Appendix A). This model returned lifetimes of 1.1 and 8.4 ns with normalized amplitudes (termed "population weights") of 0.99 and 0.01, respectively (Table 2). The population weight estimates the occupancy of a particular conformation, or a set of rapidly interconverting conformations, of pC relative to the others that are temporally resolvable, under the assumption that the conformations have equal excitation and detection efficiencies and radiative decay rates to one another. Decay components of 0.5–3 ns have been consistently observed in a variety of base-paired sequence contexts [31,34], so the dominance of the 1.1 ns component indicates that pC71 is constrained to a primarily base-paired conformation within P3. The 8.4 ns component likely arises from rare breathing events resulting in a base-stacked but unpaired conformation. No significant change in the lifetime or population weight of either component is observed when G or Hx is added. The ligand-independent emission behavior of pC71 GR, coupled with its circular dichroism (CD) spectrum be-

ing unchanged relative to the unmodified GR (Figure S3), indicates that pC substitution minimally perturbs highly structured regions within the RNA.

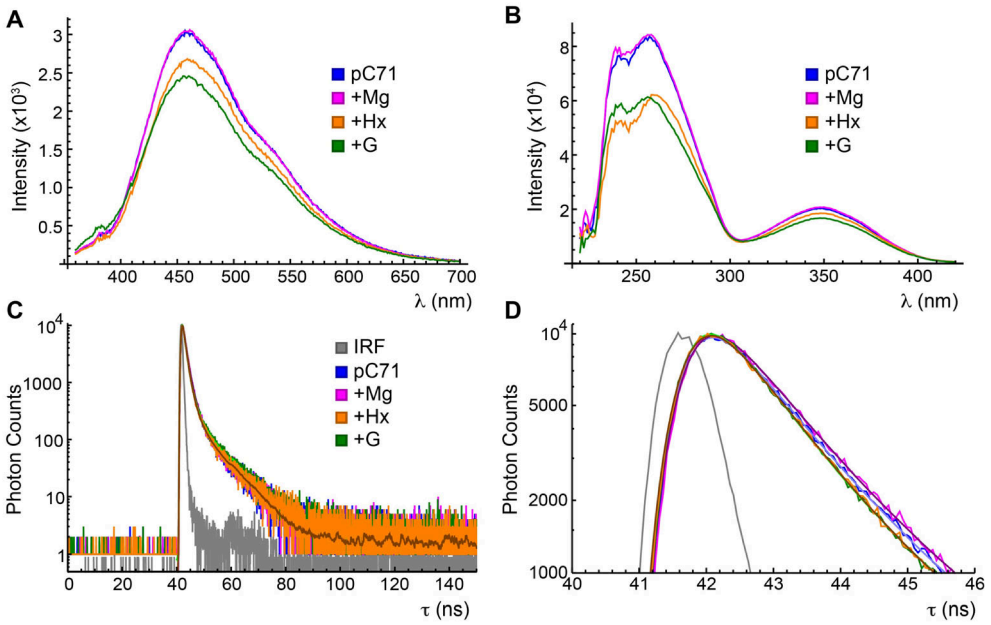


Figure 2. Steady-state and time-resolved spectroscopy of pC71 GR. (**A**) Fluorescence emission spectra of pC71 GR in standard phosphate buffer (blue), buffer supplemented with 1 mM $MgCl_2$ (magenta), buffer supplemented with 1 mM $MgCl_2$ and 310 µM Hx (orange) or buffer supplemented with 1 mM $MgCl_2$ and 4 µM G (green). (**B**) Fluorescence excitation spectra of pC71 GR. Color coding as in panel (**A**). (**C**) Fluorescence decays of pC71 GR. Color coding as in panel (**A**), with a typical instrument response function (IRF) additionally plotted in gray. $1E1G_S$ fits are overlaid in contrasting shade. (**D**) A close-up of the short-time region of panel (**C**).

Table 2. TCSPC fitting results for pC71 GR. Uncertainties represent the standard deviation across three successive data acquisitions. Unless otherwise stated, all data were collected at pH 7.4.

pC71 Condition	Model	χ^2	$\langle\tau\rangle_{obs}$ (ns)	w_1	τ_1 (ns)	w_2	τ_2 (ns)	w_3	τ_3 (ns)
Alone	$1E1G_S$	0.95	1.190 ±0.005	0.0127 ±0.0009	8.4 ±0.3	0.9873 ±0.0009 [1]	1.097 ±0.004 [1]	–	–
+1 mM Mg^{2+}	$1E1G_S$	0.96	1.24 ±0.03	0.0125 ±0.0005	8.5 ±0.2	0.9875 ±0.0005 [1]	1.15 ±0.03 [1]	–	–
+4 µM G	$1E1G_S$	1.03	1.08 ±0.01	0.014 ±0.001	8.6 ±0.2	0.986 ±0.001 [1]	0.968 ±0.006 [1]	–	–
+310 µM Hx	$1E1G_S$	0.96	1.09 ±0.01	0.0134 ±0.0004	8.0 ±0.1	0.9865 ±0.0004 [1]	1.00 ±0.01 [1]	–	–
Alone, pH 4	3E	1.28	2.3 ±0.01	0.044 ±0.003	9.1 ±0.1	0.384 ±0.004	3.52 ±0.05	0.572 ±0.006	0.97 ±0.01

[1] Parameter originates from gamma component.

2.3. Model RNAs Reveal the Photophysical Impacts of Hydrogen Bonding Between pC and G or Hx

To build a foundation for understanding the behavior of pC74 in the complex environment of the binding pocket, we investigated model 21-nucleotide single-stranded (ss) and double-stranded (ds) RNAs containing a central ApCA motif (Table 1; Figure 3). Model dsRNAs contained a central ApCA:UGU motif (termed 1:2UGU) to mimic the guanine-bound riboswitch, an ApCA:UIU motif (1:2UIU; I refers to inosine, the nucleoside with Hx as its base) to mimic the Hx-bound riboswitch, or a mismatched ApCA:UUU motif

(1:2UUU). TCSPC measurements were performed and, based on reduced χ^2 values and the behavior of the residuals (details in Appendix A), a 2E model was selected to describe the decays of the pC-labeled ssRNA St1ApCA and a 3E model was selected to describe the decays of 1:2UGU, 1:2UIU and 1:2UUU (Table 3). Under the established structural interpretation of pC fluorescence decays [34], St1ApCA exhibits a dominant (population weight of 0.7) base-stacked conformation with a lifetime of 11.9 ns and a less populated unstacked conformation with lifetime 4.6 ns.

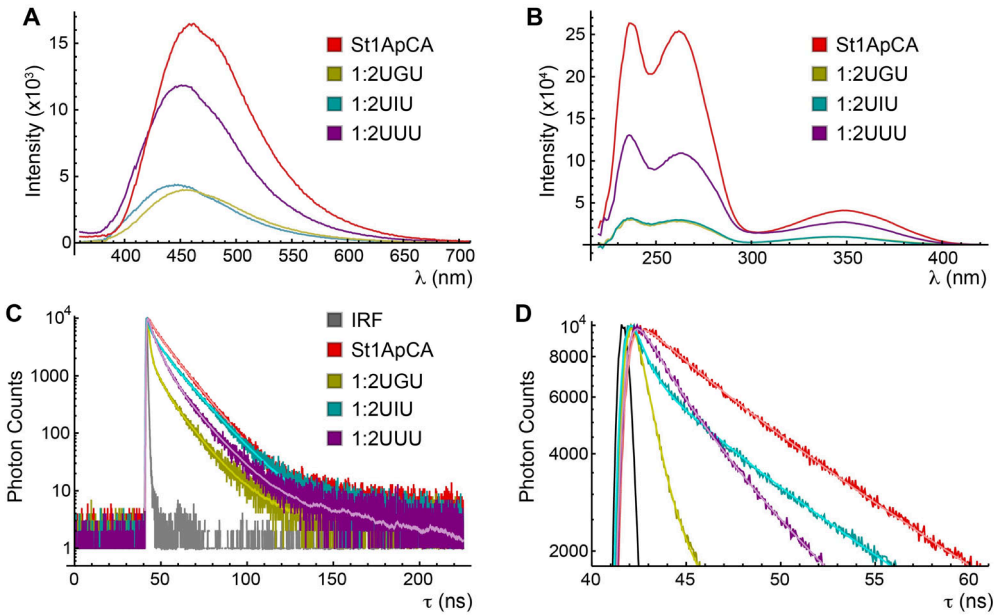


Figure 3. Steady-state and time-resolved spectroscopy of model ssRNA and dsRNAs. (**A**) Fluorescence emission spectra of St1ApCA (red), 1:2UGU (yellow), 1:2UIU (cyan) and 1:2UUU (purple). (**B**) Fluorescence excitation spectra of model RNAs. Color coding as in panel (**A**). (**C**) Fluorescence decays of model RNAs. Color coding as in panel (**A**), with a typical IRF additionally plotted in gray. 2E (for St1ApCA) or 3E (for all others) fits are overlaid in contrasting shade. (**D**) A close-up of the short-time region of panel (**C**).

Table 3. TCSPC fitting results for pC riboside (pCr) and model 21-mers. Uncertainties represent the standard deviation across three successive data acquisitions. Unless otherwise stated, all data were collected at pH 7.4.

RNA	Model	χ^2	$\langle\tau\rangle_{obs}$ (ns)	w_1	τ_1 (ns)	w_2	τ_2 (ns)	w_3	τ_3 (ns)
pCr	2E	1.11	1.904 ±0.005	0.015 ±0.008	5.1 ±0.8	0.985 ±0.008	1.86 ±0.01	–	–
pCr, pH 4	2E	1.07	1.878 ±0.003	0.0073 ±0.0008	7.2 ±0.4	0.9927 ±0.0008	1.839 ±0.004	–	–
St1ApCA	2E	1.27	9.71 ±0.02	0.701 ±0.002	11.90 ±0.02	0.299 ±0.002	4.56 ±0.08	–	–
1:2UGU	3E	1.12	1.83 ±0.02	0.037 ±0.003	13.4 ±0.3	0.1016 ±0.0006	5.6 ±0.3	0.862 ±0.003	0.90 ±0.02
1:2UIU	3E	1.28	4.6 ±0.2	0.230 ±0.008	13.35 ±0.08	0.193 ±0.007	5.5 ±0.1	0.58 ±0.01	0.57 ±0.04
1:2UUU	3E	1.18	5.33 ±0.01	0.138 ±0.002	13.49 ±0.08	0.51 ±0.01	5.44 ±0.03	0.35 ±0.01	1.99 ±0.06
St1ApCA, pH 4	3E	1.22	3.168 ±0.007	0.046 ±0.007	11.5 ±0.5	0.40 ±0.01	4.6 ±0.1	0.56 ±0.02	1.45 ±0.05

3E fits to the fully complementary duplexes 1:2UGU and 1:2UIU each revealed a sub-nanosecond decay component with lifetime of 0.90 or 0.57 ns and population weight of 0.86 or 0.58, respectively. These sub-ns lifetimes are within the practical lower limit of detection of the instrument (see Section 3.3.2), and have been previously reported for pC in measurements of similar time resolution [31]. We assign this component to a base-paired conformation, analogous to the dominant 0.5–3 ns components previously observed in dsRNA across several sequence contexts [31,34] and the dominant 1.1 ns component observed in pC71 GR (Table 2). All three duplexes exhibit a ~5.5 ns component with a population weight inversely related to the degree of pC hydrogen bonding: 0.10 with pC opposite G, 0.19 with pC opposite I, and 0.51 with pC opposite U. We assign this component to an unstacked conformation, analogous to the 4.4 ns component observed in St1ApCA. All three duplexes additionally exhibit a ~13 ns component that was least populated with pC opposite G (w = 0.04) and most populated with pC opposite I (w = 0.23). We assign this to a "breathed open" conformation in which pC is stacked but not base-paired, analogous to the 12 ns component observed in St1ApCA. Interestingly, the mismatched duplex 1:2UUU also exhibits a 2 ns decay component (w = 0.35), which was not previously observed with a CpCC:GUG motif [34] (discussed further below). In summary, the fluorescence decays of the dsRNAs investigated here reveal stacked and unstacked populations analogous to those observed in other model RNAs, as well as a faster decay of ≤2 ns whose population weight is related to the degree of hydrogen bonding between pC and the opposing base (opposite G > opposite I > opposite U).

2.4. pC74 Exhibits Ligand-Dependent Fluorescence Quenching and Maintains Binding Specificity

We next examine pC74, which replaces the ligand-coordinating C in the J3/1 linker (Figure 1C). As pC retains the necessary hydrogen bonding pattern (Figure 1B), we anticipated that pC74 GR would exhibit large ligand-dependent changes in its fluorescence properties. pC74 GR exhibits the expected fluorescence enhancement of pC in base-stacked conformations, resulting in a similar brightness as that observed in St1ApCA (Figures 3A and 4A). In the presence of ligand, the emission spectra of pC74 GR distinguish between G and Hx, where the reduction in overall intensity is directly related to the number of hydrogen bonds formed with the ligand (Figure 4A). The addition of a saturating concentration of G results in a ~40% decrease in intensity while Hx only induces a ~30% reduction. The emission lineshape of pC74 exhibits the suppressed red shoulder at ~470 nm that we have shown is indicative of a base-stacked or non-polar environment. There is no discernable change in the lineshape of the emission spectra in either ligand-bound complex (Figure S2C), in contrast to the blueshift and further suppression of the red shoulder observed upon hybridization of pC-labeled ssRNA into dsRNA (Figure S2E) [34].

We have previously demonstrated that the fluorescence excitation spectrum of pC exhibits signatures of the surrounding sequence context due to energy transfer from nearby native bases, which yields a distinct spectral feature around 260 nm [34]. Upon the addition of G to pC74 GR, the peak narrows with a reduction in intensity on the red edge (Figure S2D). This change, though slight, could be indicative of reduced interaction with the adjacent A residues (λ_{max} = 259 nm for adenosine monophosphate [63]) or direct energy transfer from the hydrogen-bonded G (λ_{max} = 246 nm; Figure S4), which we have previously observed in dsRNA [34]. No change is observed in this feature upon addition of G to pC71 GR (Figure S2B), supporting the notion that the subtle shift observed in pC74 GR arises from altered geometry within the binding pocket. As indicated by excitation spectra of the model 21-mers (Figure S2F), shifts in energy transfer interactions between pC and adjacent residues are more subtle in an ApCA context than previously observed in a CpCC context [34]. This is likely due to the smaller difference between the λ_{max} of the A residues flanking pC

and those of G and U residues opposite it in the duplexes studied here (λ_{max} = 252 nm for guanosine monophosphate, λ_{max} = 262 nm for uridine monophosphate). While the excitation spectrum of pC74 GR in the presence of Hx does exhibit a clear change in the λ_{max} of this peak to 262 nm (Figure 4B; Figure S2), this is likely confounded by the large absorbance of the saturating Hx and therefore larger inner filter effect correction required (Figure S4). A similar shift in the fluorescence excitation spectrum is observed upon addition of Hx to pC71 GR (Figure S2B), confirming that it does not reflect alterations in the binding pocket.

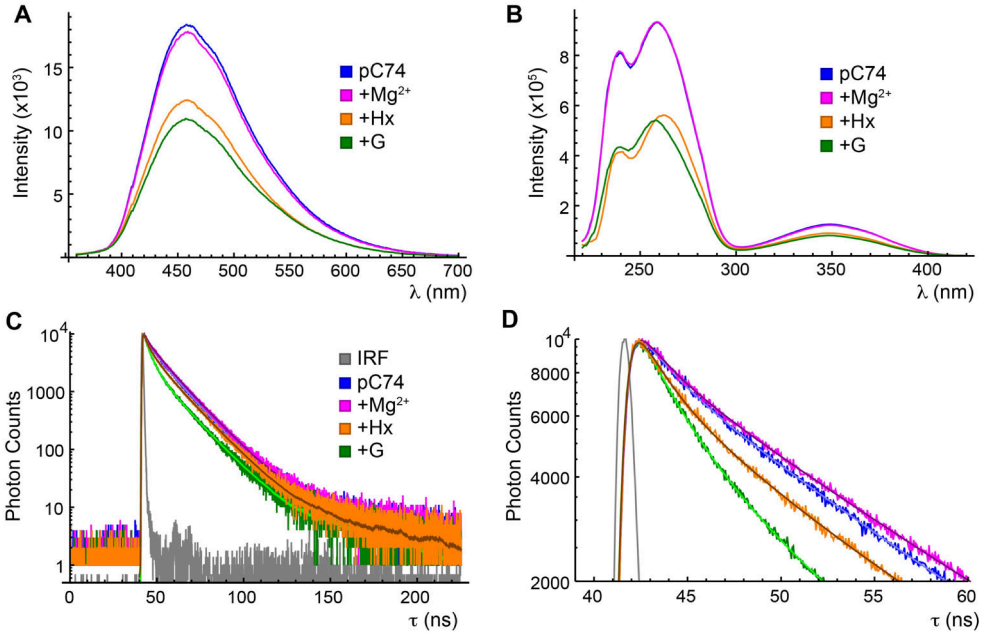


Figure 4. Steady-state and time-resolved spectroscopy of pC74 GR. (**A**) Fluorescence emission spectra of pC74 GR in standard phosphate buffer (blue), buffer supplemented with 1 mM $MgCl_2$ (magenta), buffer supplemented with 1 mM $MgCl_2$ and 310 µM HX (orange) or buffer supplemented with 1 mM $MgCl_2$ and 4 µM G (green). (**B**) Fluorescence excitation spectra of pC74 GR. Color coding as in panel (**A**). (**C**) Fluorescence decays of pC74 GR. Color coding as in panel (**A**), with a typical IRF additionally plotted in gray. 3E fits are overlaid in contrasting shade. (**D**) A close-up of the short-time region of panel (**C**).

Exploiting the fluorescence quenching exhibited by pC74 in the presence of ligand, fluorescence titrations were carried out in order to determine the K_D values for G and Hx at physiological (1 mM) and high (20 mM) Mg^{2+} concentrations for comparison with the literature (Figures 5 and S5). In 20 mM Mg^{2+}, a 4-parameter logistic (4PL) fit to maximum emission intensity vs. total ligand concentration yielded apparent K_D values of 35 ± 3 nM for G and 12.1 ± 0.2 µM for Hx (mean ± standard deviation across three experimental replicates). K_D values for the A21U/U75A mutant of the GR were previously determined via isothermal titration calorimetry in 10 mM Mg^{2+}, and were found to be 3 nM for G and 3.3 µM for Hx [56]. The authors noted no change in the binding affinity at higher concentrations of Mg^{2+}. In 1 mM Mg^{2+}, pC74 exhibited apparent K_D values of 80 ± 10 nM for G and 41 ± 4 µM for Hx. Substitution of pC at position 74 in an A21U/U75A background thus modestly decreases the binding affinity while maintaining apparent K_D values of the same order of magnitude and high specificity for G over Hx. It should be noted that the actual K_D values for G are likely lower than the K_{app} values obtained from the 4PL fits, as significant depletion of G is likely to occur with the 150 nM RNA concentration utilized here (see Section 3.3.1). Indeed, analysis using a quadratic model that accounts for mass balance [20,64] suggests smaller K_D values under both physiological and high

Mg^{2+} concentrations, though the much higher RNA concentration limits the precision of these estimates. Additionally, controls were carried out, in which G or Hx was titrated into pC riboside (pCr). pCr exhibited no change in emission intensity under all conditions (Figure S6), confirming that the decrease in fluorescence observed with pC74 is due to ligand binding rather than photodamage or nonspecific interactions between pC and ligand. In summary, while pC74 GR shows a modest reduction in ligand-binding affinity compared to unlabeled GR, it maintains high specificity, including under physiological conditions where the low Mg^{2+} concentration might exacerbate any defects induced by pC labeling. This preservation of key functions exhibited by unmodified GR suggested that pC74 GR could provide meaningful information about structure and ligand binding through further spectroscopic studies.

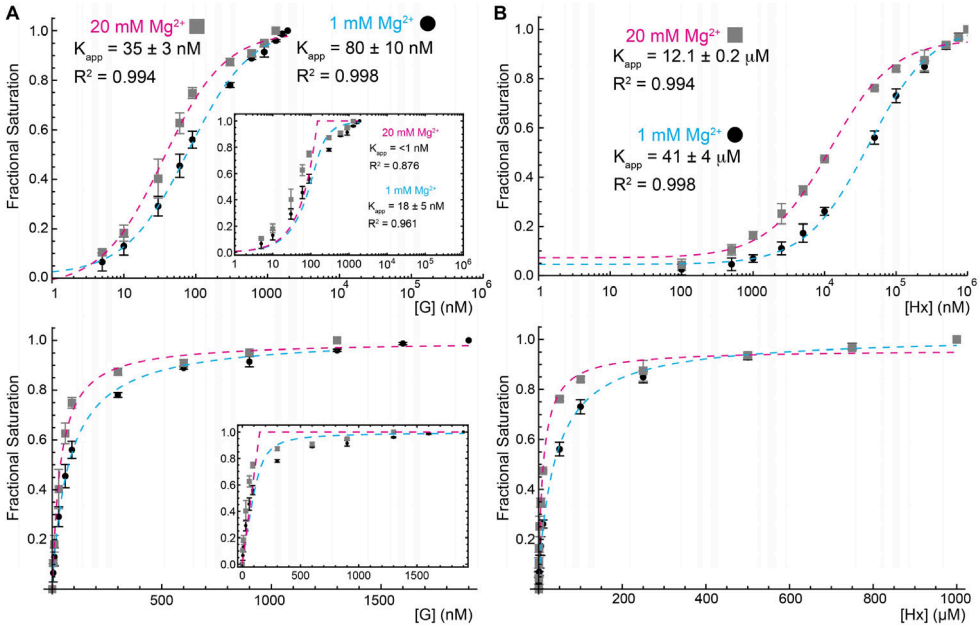


Figure 5. Ligand titrations. Error bars represent the standard deviation across three experimental replicates. (**A**) Titration of G into pC74 GR in phosphate buffer supplemented with 1 mM $MgCl_2$ (black; fit in dashed blue) or 20 mM $MgCl_2$ (gray; fit in dashed pink). Fractional saturation was computed from the peak intensity of the emission spectrum at each ligand concentration and then fitted with a 4-parameter logistic equation with the Hill coefficient fixed at 1, as a function of total ligand concentration. Top: logarithmic scale on x-axis. Bottom: linear scale on x-axis. Insets: Titration curves fitted with a quadratic model to account for ligand depletion (see Section 3.3.1). (**B**) 4PL fits as in panel (**A**) but with Hx titrated into pC74 GR.

2.5. Conformational Ensemble of pC74

TCSPC allows for a greater examination of the conformations that pC74 samples within the binding pocket and how they give rise to the distinct emission behaviors of the G- and Hx-bound complexes. All pC74 GR decays were well fit by a 3E model (χ^2 = 1.17–1.23; details in Appendix A), returning short, intermediate, and long decay components with shifting lifetimes and population weights between conditions (Figure 4C,D; Table 4). All conditions measured (RNA alone, +1 mM Mg^{2+}, +4 μM G or +310 μM Hx) exhibit a 14 ns component, which is attributed to a base-stacked and unpaired state. In the absence of ligand, this stacked state is the predominant conformation (RNA alone, w = 0.44; RNA + 1 mM Mg^{2+}, w = 0.51). When saturating concentrations of ligand are introduced, this population decreases by an amount commensurate with the degree of hydrogen bonding to the ligand (G, w = 0.21; Hx, w = 0.36), as was observed in the model 21-mers when St1ApCA is hybridized to complementary strands with different bases opposite pC (Table 3). In addition,

all conditions measured exhibit an intermediate length decay component, which changes in length from 7 ns in the ligand-free state to 5.5 ns in the presence of either ligand without meaningfully changing in population (w ≈ 0.30). This is assigned as an unpaired and unstacked state, observed in the corresponding 21-mers at 5.5 ns. Both ligands induce a shift in population to a short decay component, attributed to the base-paired and base-stacked state. In the presence of G, this 2 ns component becomes the predominant population (w = 0.45). In the presence of Hx, this population is equal in weight to the base-stacked and unpaired state (w = 0.34) and, at 1.5 ns, is more rapidly decaying than that of the G-bound pC74 GR. Thus, the lifetime of this state is inversely related to the degree of pC's hydrogen bonding, a pattern that was also observed in the model double-stranded 21-mers (Table 3).

Table 4. TCSPC fitting results for pC74 GR. Uncertainties represent the standard deviation across three successive data acquisitions. Unless otherwise stated, all data were collected at pH 7.4.

pC74 Condition	Model	χ^2	$\langle\tau\rangle_{obs}$ (ns)	w_1	τ_1 (ns)	w_2	τ_2 (ns)	w_3	τ_3 (ns)
Alone	3E	1.21	8.89 ±0.07	0.44 ±0.02	14.1 ±0.2	0.32 ±0.02	7.0 ±0.04	0.234 ±0.005	1.6 ±0.1
+1 mM Mg^{2+}	3E	1.19	9.45 ±0.06	0.51 ±0.02	14.25 ±0.09	0.26 ±0.01	7.2 ±0.3	0.231 ±0.006	1.57 ±0.08
+4 µM G	3E	1.17	5.80 ±0.04	0.21 ±0.01	14.3 ±0.2	0.34 ±0.03	5.4 ±0.4	0.45 ±0.04	2.1 ±0.2
+310 µM Hx	3E	1.23	7.19 ±0.08	0.358 ±0.006	14.10 ±0.09	0.301 ±0.007	5.5 ±0.3	0.34 ±0.01	1.4 ±0.1
Alone, pH 4	3E	1.27	3.54 ±0.03	0.069 ±0.004	15.3 ±0.3	0.338 ±0.009	5.2 ±0.2	0.59 ±0.01	1.22 ±0.06

Unexpectedly, pC74 GR also exhibited a 1.5 ns decay component (w = 0.24) in the absence of ligand. Though this timescale has typically been observed in base-paired contexts [31,34], it was also present in the mismatched dsRNA 1:2UUU (w = 0.35, $\boldsymbol{\tau}$ = 1.99; Table 3), demonstrating that a component of this length can arise without base pairing. In order to establish the conformation underlying this rapidly decaying population in pC74 GR, we performed measurements under acidic conditions to compare the fluorescence properties of denatured pC-labeled GR with those observed at pH 7.4 (Figure 6). HCl has been used previously to rapidly denature RNA [65], and the concentration required to achieve denaturation of the GR (determined by CD to occur at pH 4; Figure S7) altered the buffer conditions only by increasing the total chloride concentration from 100 mM to 117 mM. While the fluorescence decay of pC74 GR at pH 4 is still well fit by a 3E model (χ^2 = 1.27), stark changes in the occupancy of the states described above are observed (Table 4). The 15 ns base-stacked population decreases drastically at pH 4 to a weight of only 0.07, while the shortest decay component becomes dominant (w = 0.59) with a slight reduction in length to 1.2 ns (Figure 6D). The increased population of this rapidly decaying state is reflected in a 67% decrease in the emission intensity (Figure 6A). In contrast, pC71 GR exhibits a 67% increase in emission intensity at pH 4, resulting in a nearly identical emission intensity and lineshape to pC74 (Figure 6B,C). This confirms that the strong emission of pC74, the weak emission of pC71, and its distinctive ~530 nm shoulder all reflect unique environments within the native riboswitch structure. At pH 4, pC71 GR required a 3E fit (χ^2 = 1.28), in contrast to the 1E1G_S model that was optimal under neutral conditions. As in pC74 GR, the shortest decay component (0.97 ns) dominates with a population weight of 0.57 (Table 2). This same shift is observed in St1ApCA, which also required a 3E fit under acidic conditions, as opposed to the 2E fit that was adequate under neutral conditions. Notably, the new component identified by the 3E model (1.5 ns; w = 0.56) closely mimics

both the lifetime and the population weight of the short component observed in pC71 GR and pC74 GR at pH 4.

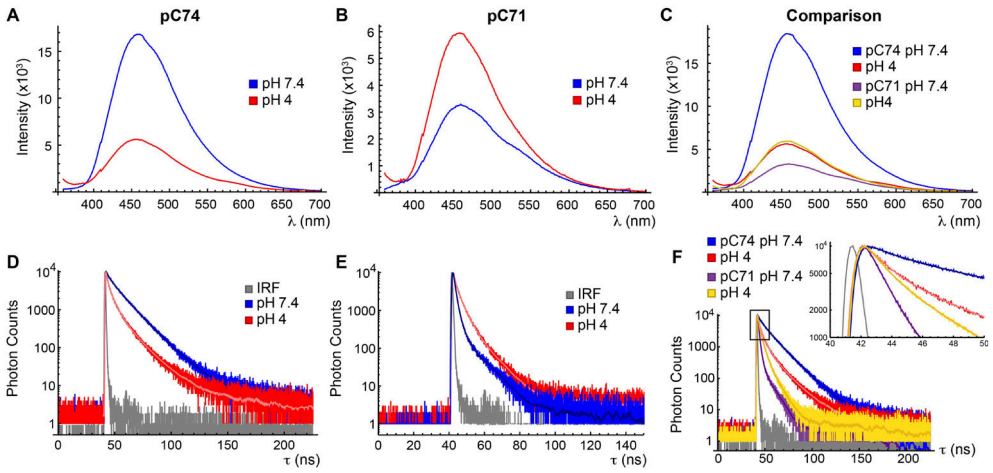


Figure 6. Steady-state and time-resolved spectroscopy of pC74 and pC71 GR under native (pH 7.4) and denaturing (pH 4) conditions. (**A**) Fluorescence emission spectra of pC74 in standard phosphate buffer at pH 7.4 (blue) or phosphate buffer adjusted to pH 4 using HCl (red). (**B**) Same as panel (**A**) for pC71 GR. (**C**) Overlaid emission spectra of pC74 GR at pH 7.4 (blue) and pH 4 (red) and pC71 GR at pH 7.4 (purple) and pH 4 (yellow). (**D**) Fluorescence decays of pC74 GR at pH 7.4 (blue) and pH 4 (red). 3E fits are overlaid in contrasting color. (**E**) Fluorescence decays of pC71 GR at pH 7.4 (blue) and pH 4 (red). 1E1G$_S$ (pH 7.4) and 3E (pH 4) fits are overlaid in contrasting color. (**F**) Overlaid fluorescence decays of pC74 GR at pH 7.4 (blue) and pH 4 (red) and pC71 GR at pH 7.4 (purple) and pH 4 (yellow). Inset: Close-up of short-time region.

Free pCr exhibits a vastly dominant (w = 0.99) lifetime of 1.8 ns under both neutral and acidic conditions (Table 3, Figure S8), representing the characteristic lifetime of pC in a completely unstacked and unpaired environment. We therefore propose that under denatured conditions, pC71, pC74 and the pC label within St1ApCA are all able to significantly populate a "riboside-like" state of pC, more broadly termed an "extrahelical conformation" [66,67]. Extrahelical conformations have been observed for 2-AP in mismatched [66] and fully complementary [68] DNA duplexes, as well as riboswitches [20]. As we propose here for pC, extrahelical conformations of 2-AP are distinguished by fluorescence lifetimes comparable to free nucleosides. As the lifetimes of pCr and the short component of pC74 GR are nearly independent of pH (Figure S8; Tables 3 and 4), this suggests that in the absence of ligand under native conditions, pC74 is able to sample an extrahelical conformation in which it is completely flipped out from the J3/1 linker. This state is then overcome by the characteristic, higher population weight conformation of pC74 hydrogen-bonded to ligand. 1:2UUU is similarly able to sample an extrahelical conformation (the previously mentioned 2 ns decay component) that is overcome by the rapidly decaying base-paired states present in the fully complementary dsRNAs 1:2UGU and 1:2UIU. The presence of an extrahelical conformation of 1:2UUU, in addition to its substantial population of the 5.5 ns "unstacked" conformation, indicates that the mismatched, AU-rich core of 1:2UUU has a locally weaker base-stacking stability than the other duplexes investigated here or previously [34]. As the lifetimes of the extrahelical and base-paired conformations of pC are similar to each other, control measurements and structural information obtained by complementary methods should be leveraged in order to accurately assign decay components with lifetimes of 0.5–2 ns to molecular conformations.

2.6. FDCD Reveals Ligand-Induced Quenching of Base-Stacked Conformations

We next utilized CD and fluorescence-detected CD (FDCD) spectroscopy to investigate the local and global conformations adopted by pC74 GR in response to Mg^{2+} and ligand. The standard CD spectra revealed a lineshape characteristic of A-form dsRNA [69–71], with a prominent positive feature at ~265 nm and a prominent negative feature at ~210 nm, and no changes were observed upon addition of Mg^{2+}, G or Hx (Figure 7). This is consistent with the pre-organization of the riboswitch into a global structure dominated by three base-paired helical domains (P1, P2 and P3) [52]. While pC has the potential to generate a CD signal in its longest-wavelength band [72], this was unresolvable in the standard CD spectra due to its low amplitude and partial spectral overlap with the strong CD signal generated by the 68 native bases in pC74 GR (Figure 7). CD was therefore unable to report on the local environment around the labeling site.

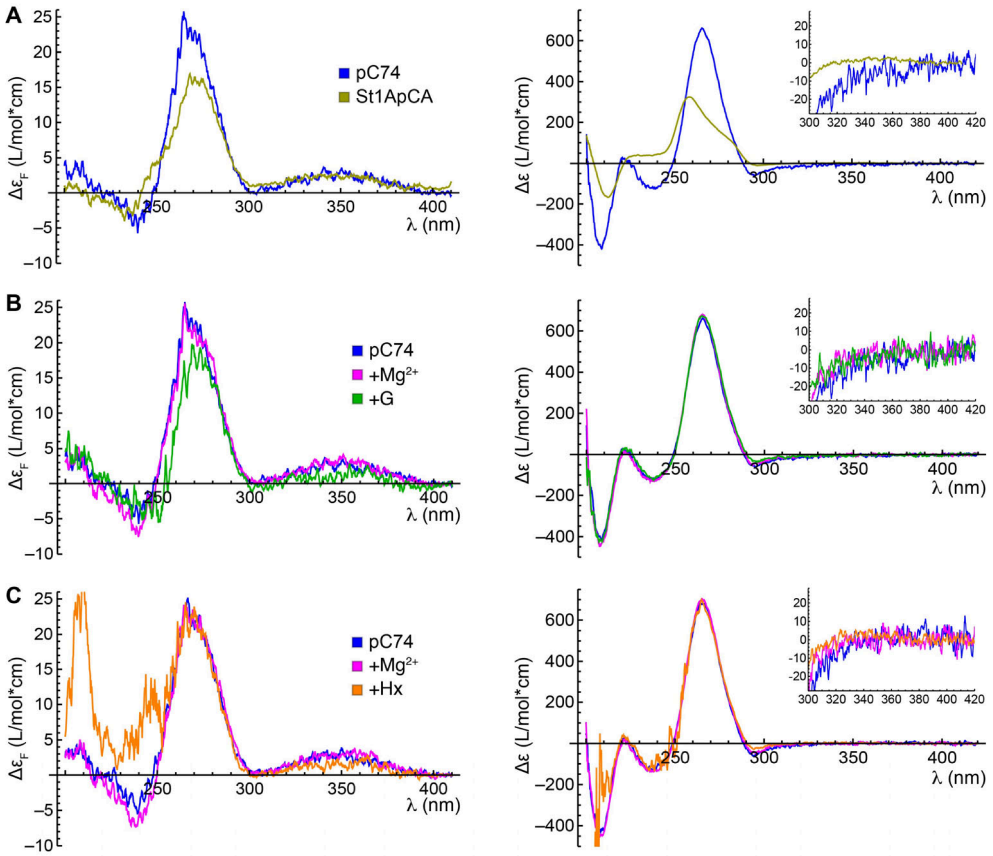


Figure 7. CD and FDCD spectroscopy of pC74 GR. (**A**) FDCD (left) and CD (right) spectra of pC74 GR (blue) and St1ApCA (yellow) in standard phosphate buffer. The inset shows a close-up of the long-wavelength region. (**B**) FDCD (left) and CD (right) spectra of pC74 GR in standard phosphate buffer (blue), buffer supplemented with 1 mM $MgCl_2$ (magenta) or buffer supplemented with 1 mM $MgCl_2$ and 4 μM G (green). (**C**) FDCD (left) and CD (right) spectra of pC74 GR in standard phosphate buffer (blue), buffer supplemented with 1 mM $MgCl_2$ (magenta) or buffer supplemented with 1 mM $MgCl_2$ and 310 μM Hx (orange).

FDCD reveals the CD signals that arise from conformations of an RNA that exhibit bright pC fluorescence. These signals can be generated by electronic transitions on pC itself, transitions delocalized across pC and native bases, and energy transfer from native bases to pC [73]. As previously observed in pC-labeled trinucleotides and ssRNA [34], the FDCD spectra of St1ApCA and pC74 GR both exhibit a positive feature in the longest-wavelength absorption band of pC and a sigmoidal feature at shorter wavelengths arising

from excitation of nearby native bases followed by energy transfer to pC. The spectra differ in their details, however, due to the unique structure of the binding pocket surrounding pC74. Most notably, the intensity of the short-wavelength feature is higher in pC74 GR than in St1ApCA, suggesting that a larger number of bases participate in energy transfer to pC74, and its lineshape also differs, reflecting the difference in structure surrounding pC (Figure 7A).

The intensity of a short-wavelength negative feature becomes slightly but reproducibly larger upon addition of Mg^{2+} to pC74 GR, and the intensity of the entire FDCD spectrum becomes significantly lower upon addition of a saturating concentration of G (Figure 7B). This shows that binding of G has the effect of quenching emission from the conformational subpopulations in which pC and nearby native bases have the strongest CD signals, while subpopulations with weaker CD remain bright. TCSPC revealed that a dominant effect of the ligand is to shift population from a base-stacked but unpaired conformation to a stacked and paired conformation (Table 4). Thus, the ensemble of base-stacked conformations becomes dominated by the darker, ligand-bound state in the presence of G, consistent with the reduction in FDCD intensity upon ligand binding. Addition of Hx induces a smaller reduction in FDCD than G in the longest-wavelength band, consistent with the smaller shift in population from bright to dark base-stacked conformations observed by TCSPC. Changes also occur in the short-wavelength feature, but their nuances are likely distorted by imperfect correction for the strong inner filter effect generated by saturating concentrations of Hx (Figure S4), which also impacted the fluorescence excitation spectra discussed above.

2.7. Stopped-Flow Fluorescence Spectroscopy Reveals Differences in Ligand Association Rates

Previous studies have utilized 2-AP as a ligand analogue for fluorescence studies of GR variants, exploiting the fact that their affinities for 2-AP were proportional to, albeit much weaker than, their affinities for G [42]. Furthermore, 2-AP has been used as a ligand analogue in stopped-flow fluorescence studies of ligand binding to a naturally occurring adenine-sensing riboswitch [40] and a mutant of GR designed to preferentially bind adenine (C74U) [41]. In order to determine if pC could be utilized for kinetic studies of ligand binding, we carried out stopped-flow fluorescence measurements on pC74 GR where increasing concentrations of either G or Hx were introduced (Figure 8). The ligand-dependent quenching of pC74 allowed observed association rates to be determined from the decrease in fluorescence intensity over time. All measurements were carried out under pseudo-first-order conditions, with pC74 GR at 55 nM and ligand in a large excess (275 to 2750 nM G; 50 to 500 µM Hx). The fluorescence traces were scaled to run from a maximum of 1 to a minimum of 0. These corrected traces were fitted with a bi-exponential function, and the observed association rates (k_{obs}) were calculated as a weighted average of the fast and slow decay components' rate constants (Figure S9, individual weights and rate constants in Table S1). As previously done for 2-AP binding to C74U GR [41], the association rate (k_{assoc}) was estimated as the slope of a linear fit to k_{obs} vs. ligand concentration (Figure 8). pC74 exhibited clear time-dependent fluorescence quenching upon introduction of both G and Hx. Far slower changes were observed when buffer was introduced or when ligand was introduced to pCr (Figure S9C–E), indicating that quenching of pC74 emission after rapid mixing arises from ligand binding. As expected, Hx required much higher concentrations to achieve the same degree of fluorescence quenching as G, which is reflected in their k_{assoc} values: G = 4.1×10^4 $M^{-1}s^{-1}$ (standard error from linear fit: 0.2×10^4 $M^{-1}s^{-1}$); Hx = 0.033×10^4 $M^{-1}s^{-1}$ (standard error: 0.003×10^4 $M^{-1}s^{-1}$). Interestingly, the k_{assoc} value of G is nearly identical to the rate determined for 2-AP binding to the C74UGR at 1.25 mM Mg^{2+} (4.4×10^4 $M^{-1}s^{-1}$) [41]. The necessity of a bi-exponential fit may reflect a previously proposed binding model in which GR samples were in "closed" and "open"

states, where only the latter is capable of binding to a ligand [41,42]. These results confirm that pC substitutions can be used to reliably measure binding kinetics between RNA and small-molecule ligands.

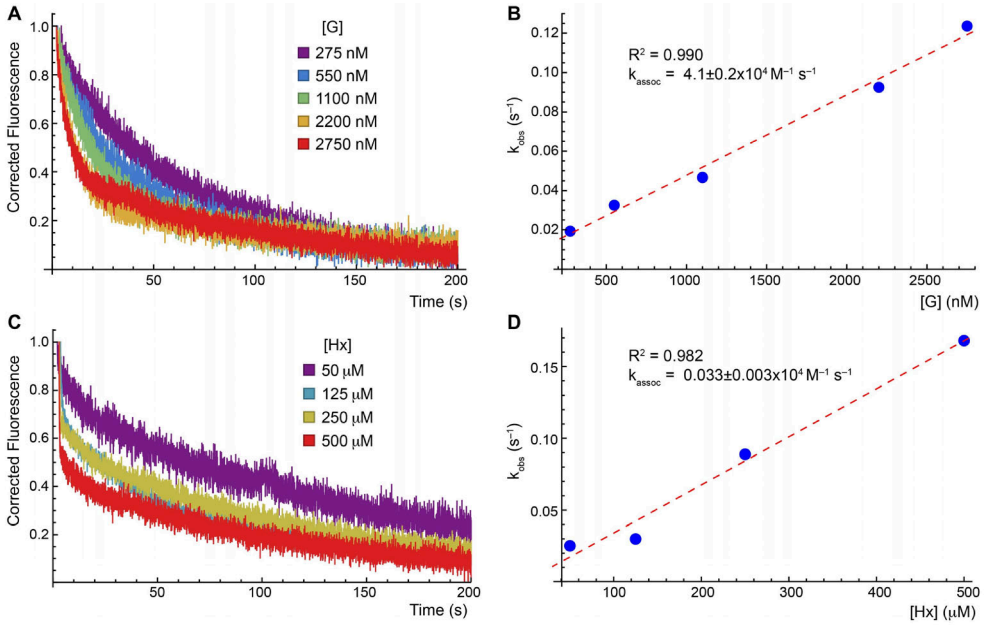


Figure 8. Stopped-flow fluorescence spectroscopy. (**A**) Corrected fluorescence traces for the association of 275 nM (purple), 550 nM (blue), 1100 nM (green), 2200 nM (yellow) or 2750 nM (red) G to pC74 GR. Raw fluorescence was corrected to run from a maximum of 1 (representing the fluorescence of ligand-free pC74 GR) to a minimum of 0 (fluorescence of ligand-bound pC74 GR). See Section 3.3.4 for data processing details. (**B**) The observed rate constant plotted as a function of G concentration. A linear fit (red) returned an association rate constant of 4.1×10^4 $M^{-1}s^{-1}$. The reported uncertainty of k_{assoc} ($\pm 0.2 \times 10^4$ $M^{-1}s^{-1}$) is the standard error of the slope obtained from the linear fit. (**C**) Corrected fluorescence traces for the association of 50 µM (purple), 125 µM (blue), 250 µM (yellow), or 500 µM (red) Hx to pC74 GR. (**D**) The observed rate constant plotted as a function of Hx concentration. A linear fit (red) returned an association rate constant of 0.03×10^4 $M^{-1}s^{-1}$. The reported uncertainty of k_{assoc} ($\pm 0.003 \times 10^4$ $M^{-1}s^{-1}$) is the standard error of the slope obtained from the linear fit.

3. Materials and Methods

3.1. Reagents

RNA oligonucleotides were purchased from Horizon Discovery (Dharmacon; Cambridge, UK) and DNA oligonucleotides were purchased from Integrated DNA Technologies (IDT; Coralville, IA, USA) (Table 1) and deprotected and desalted by the manufacturer. The GR RNA sequence was split into a 5′ and a 3′ segment. pC71, pC74 and unmodified versions of the 3′ segment were all purchased with a 5′ phosphate. In addition, pC-labeled 3′ segments and all 21-mers were high-pressure liquid chromatography-purified by the manufacturer. Oligonucleotide stock solutions were prepared in DEPC-treated water and the A260 was used to determine the concentration using the extinction coefficient provided by the manufacturer. pCr (PYA11092-B010) was obtained from Biosearch Technologies (Novato, CA, USA) and prepared in MilliQ H_2O at a concentration of 5 mM. G (G11950-10G) was obtained from Sigma Aldrich (Burlington, MA, USA) and prepared in 0.4 M HCl at a concentration of 3 mM. Hx (H9377-5G) was obtained from Sigma Aldrich and prepared in 50 mM NaOH at a concentration of 53 mM. Buffers used for spectroscopy were prepared in MilliQ H_2O and sterile-filtered prior to use.

3.2. Riboswitch Preparation

Full-length GR samples were prepared via splint-mediated ligation utilizing T4 RNA ligase 2 (T4RL2-100; Molecular Cloning Laboratories, San Francisco, CA, USA). Five nanomoles of each of the 5′ segment, the 3′ segment, and DNA splint (Table 1) were combined and heated at 90 °C for 2 min and cooled at RT for 10 min. 10x T4 RNA ligase 2 buffer (500 mM Tris-HCl, 20 mM $MgCl_2$, 10 mM DTT, pH 7.5 @ 25 °C) was added to a concentration of 1x after 30 s of cooling. Once cooled, sufficient buffer was added to reach a final concentration of 1x in the complete reaction, ATP to a final concentration of 200 µM and water to a final volume of 150–175 µL as required to accommodate the volumes of oligonucleotide. After mixing, 60 units of T4 RNA ligase 2 were added. The reactions were incubated at RT for 3 h, then quenched with 2x formamide loading buffer (90% formamide, 1x TBE) and stored at −20 °C overnight. The reactions were then run on a 10% polyacrylamide, 8 M urea gel. The RNA was recovered from the product band via the crush and soak method or electroelution using a BioRad (Hercules, CA, USA) model 422 electro-eluter, followed by ethanol precipitation in the presence of 300 mM NaOAc.

3.3. Spectroscopy

Unless otherwise noted, all spectra were collected at 20 °C in a buffer consisting of 20 mM Na_iPO_4 (pH 7.4) and 100 mM NaCl (termed "standard buffer"). GR and 21-mers were annealed before measurement by heating at 90 °C for two minutes then cooled at RT for 10 min. Where noted, $MgCl_2$, G and/or Hx were added after cooling. Experiments under acidic conditions were performed by preparing samples in standard buffer and then adding HCl to achieve a pH of 4. Samples were incubated at RT for five minutes after addition of the ligand or other solvent components. Analysis was carried out in Mathematica (v12.3.1.0; Wolfram Alpha, Champaign, IL, USA) unless otherwise stated.

3.3.1. Steady-State Absorbance and Fluorescence Spectroscopy

Steady-state spectra were collected on an Edinburgh Instruments (Edinburgh, UK) FS5 spectrofluorometer with a 1 nm step size and a 1 s dwell time. Fluorescence titrations were collected with GR or pCr at a concentration of 150 nM. The fractional saturation (FS) was computed from the peak fluorescence intensity (I_{max}) at each ligand concentration (Equation (1)), plotted as a function of total ligand concentration, and fitted with a 4PL (Equation (2); Hill coefficient fixed at 1) or quadratic (Equation (3)) binding model. Reproducibility suffered at RNA concentrations lower than 150 nM due to low emission intensity. As such, apparent K_D values below or around 150 nM obtained from a 4PL model represent the maximum possible value.

$$FS_i = \frac{F_i - F_0}{F_f - F_0} \quad (1)$$

In Equation (1), F_i represents the I_{max} value at ligand concentration i, F_0 represents the I_{max} value in the absence of ligand, and F_f represents the I_{max} value at the highest measured ligand concentration.

$$FS = \frac{a - d}{1 + \left(\frac{x}{K_D}\right)^b} \quad (2)$$

In Equation (2), a and d represent the minimum and maximum values of the curve and b represents the Hill coefficient.

$$FS = \frac{(K_D + R + L) - \sqrt{(K_D + R + L)^2 - 4RL}}{2R} \quad (3)$$

In Equation (3), R represents the RNA concentration and L represents the ligand concentration.

All other steady-state spectra were collected at an RNA concentration of 1 μM. Emission spectra were recorded by exciting at 340 nm with a 5 nm bandwidth while scanning from 360 to 700 nm with an emission bandwidth of 5 nm for fluorescence titrations or 2 nm for all other steady-state spectra. Excitation spectra were recorded by monitoring emission at 460 nm with a 5 nm bandwidth while scanning from 220 to 420 nm with a 2 nm excitation bandwidth. 21-mer and GR excitation spectra were corrected for the inner filter effect using absorbance spectra collected under the same conditions.

3.3.2. TCSPC

TCSPC measurements were collected on a Horiba (Irvine, CA, USA) Fluoromax-5 with a TemPro fluorescence lifetime system equipped with a 340 nm NanoLED excitation source (1 MHz repetition rate). Fluorescence decays were collected to a peak count of 10,000 across a 200 ns window with bins of 55 ps. A 420 nm long-pass filter was placed in the emission path while neutral density filters were placed in the excitation path with sufficient optical density to avoid pulse pile up. Instrument response functions (IRFs) were collected by acquiring data on buffer with no long-pass filter in place.

Decays were analyzed by iterative reconvolution fitting in Matlab (R2024a) using open-source software [74], as previously described [34]. Upon fitting with a constant IRF background of 0 counts, a timing shift between the IRF and decays of ~50 ps was returned. Under ideal conditions, decays with time constants of ~1/10 the full width at half maximum (FWHM) of the IRF can be recovered, with the lower limit determined by the bin width and timing shift. As the FWHM of the IRF was ~850 ps in the measurements reported here, the shortest components (~600 ps) are well within this lower limit.

The observed average lifetime was calculated as an amplitude-weighted average of the lifetimes obtained from exponential or gamma distribution parameters (Equation (4)).

$$\langle \tau \rangle_{obs} = \sum_{i=1}^{n} w_i \cdot \tau_i \quad (4)$$

A gamma component's time constant was defined as the mean of the gamma distribution (Equation (5)), as in analysis of other FBAs [62].

$$\langle \tau_i \rangle = \frac{1}{\alpha_i \cdot \kappa_i} \quad (5)$$

3.3.3. CD and FDCD

CD and FDCD spectra were recorded as previously described [34,75] on a JASCO Inc. (Tokyo, Japan) J1500 circular dichroism spectrometer with an FDCD-551 attachment and a 420 nm long-pass filter placed in front of the emission detector. FDCD scans were collected at an excitation bandwidth of 4 nm and a scanning speed of 20 nm/min with a 4 s digital integration time over the range 200–410 nm. The gain on the emission detector was set such that the maximum signal in the DC measurement channel was ~1 V. FDCD spectra of GR were collected with RNA at a concentration of 200 nM, requiring 20 accumulations to be averaged for a sufficient signal-to-noise ratio. St1ApCA was measured at a concentration of 1 μM, requiring 10 accumulations. CD scans were collected under the same conditions out to 420 nm, only requiring 3 accumulations.

CD spectra were background-corrected using buffer scans and converted to units of Δε (L/mol*cm). FDCD spectra were background-corrected using sodium fluorescein in water at concentrations allowing for similar detector gain to each pC sample [34,76]. Sample and fluorescein scans were corrected with buffer and water, respectively. θ_F was calculated by dividing the FDCD channel by the DC channel. θ_F of fluorescein was smoothed with a Weiner filter (r = 15) and then subtracted from θ_F of the corresponding sample.

Established theory [73] was used to convert θ_F to the quantity $\Delta\varepsilon_F$ (Equation (6)), analogous to the typical and readily interpretable units of CD, Δε (L/mol*cm).

$$\Delta\varepsilon_F = \varepsilon_F\left(\frac{\theta_F}{14323} + \frac{CD}{32980 \cdot A} + \frac{ln(10) \cdot CD \cdot 10^{-A}}{32980(1-10^{-A})}\right) \quad (6)$$

ε_F was approximated by dividing the DC signal at each wavelength by the measured Xe lamp intensity and then corrected for the inner filter effect using the corresponding absorbance spectrum. These excitation spectra were converted to units of L/mol*cm by scaling the value at 347 nm to match that as previously reported [77].

3.3.4. Stopped-Flow Fluorescence Spectroscopy

Stopped-flow fluorescence measurements were performed on an Edinburgh Instruments FS5 spectrofluorometer using an SFA-20 Rapid Kinetics Accessory equipped with a pneumatic drive attachment. RNA was prepared at a concentration of 110 nM in standard buffer + 1 mM MgCl, resulting in a final concentration of 55 nM after mixing. Ligands were prepared at 2x the desired final concentration in standard buffer + 1 mM $MgCl_2$. Fluorescence intensity was monitored at 460 nm with a 10 nm bandwidth under continuous excitation at 340 nm with a 10 nm bandwidth. Traces were collected over 200 s (G) and 300 s (Hx) with a time resolution of 30 and 40 ms, respectively. Each line of the flow circuit was rinsed with 10 mL of water before priming with its corresponding RNA, buffer, or ligand solution. The ligand line was rinsed with 10 mL of water in between ligand concentrations.

Fluorescence intensity traces were corrected to run from 1.0 to 0 (Equation (7)) before fitting with a bi-exponential function (Equation (8)). Quality of fit was assessed by R^2 and the results are reported in Table S1. The observed rate constant (k_{obs}) was calculated as a weighted average of the two rate constants (Equation (9)). A_i represents the raw amplitude returned from the bi-exponential fit, k_i represents the corresponding rate constant, and I_0 represents a constant y-offset.

$$F_{i,C} = \frac{F_i - F_{min}}{F_{max} - F_{min}} \quad (7)$$

$$I = I_0 + A_1 e^{-k_1 t} + A_2 e^{-k_2 t} \quad (8)$$

$$k_{obs} = \frac{A_1 k_1 + A_2 k_2}{A_1 + A_2} \quad (9)$$

3.4. Computational Methods

All calculations were carried out in Gaussian09 [78] (Gaussian, Inc., Wallingford, CT, USA). Methods and basis sets were selected based on the recommendations for pC-containing systems presented in Nguyen et al. [79]. First, the ground state molecular geometries of A, U, and pC nucleobases were optimized at the MP2/6–31G(d,p) level. Using previously published coordinates for A-form trinucleotides [32] or the corresponding GR crystallographic coordinates (PDB: 4FE5 (ApCA) [45], 2EES (ApCU) [53]), the optimized monomers were assembled into ApCA, ApCU, and UpCU trimers for further calculations. Configuration interaction singles with perturbative second-order corrections [CIS(D)] at the aug-cc-pVDZ level of theory was used to calculate the vertical excitation energy of the first 10 excited states. For each excited state, the natural transition orbitals were calculated at the same level of theory.

4. Conclusions

In summary, we have demonstrated the use of pC as a multifaceted, minimally perturbing probe that can report on the conformations sampled by specific nucleotides within a riboswitch and can act as a direct sensor of ligand binding. The ligand-dependent quenching of pC74 enabled the analysis of many aspects of GR structure and function, such as its

affinity for various ligands, the conformational ensemble within the binding pocket, and the kinetics of ligand binding. We show that pC substitution preserves essential properties of the GR even when it replaces a critical ligand-binding residue, such as distinct binding affinity and kinetics determined by the number of hydrogen bonds formed with the ligand. We show that pC can sample base-stacked, unstacked, extrahelical and hydrogen-bonded conformations within the complex environment of the binding pocket, which exhibit varying degrees of fluorescence quenching or enhancement. These findings establish a framework for the broader use of pC in complex RNAs of biological and technological interest.

Supplementary Materials: The following supporting information can be downloaded at https://www.mdpi.com/article/10.3390/ijms27219651/s1.

Author Contributions: Conceptualization, T.L.C. and J.R.W.; methodology, T.L.C.; formal analysis, T.L.C.; investigation, T.L.C. and G.A.V.; writing—original draft preparation, T.L.C. and J.R.W.; writing—review and editing, G.A.V.; visualization, T.L.C. and J.R.W.; supervision, J.R.W.; project administration, J.R.W.; funding acquisition, J.R.W. All authors have read and agreed to the published version of the manuscript.

Funding: This research was funded by the National Science Foundation, grant number 2338251 (Division of Chemistry and Division of Molecular and Cellular Biology), and by the University of Oregon Office of the Vice President for Research and Innovation via the Molecular Biology and Biophysics Training Program.

Institutional Review Board Statement: Not applicable.

Informed Consent Statement: Not applicable.

Data Availability Statement: The original contributions presented in this study are included in the article/Supplementary Material. Further inquiries can be directed to the corresponding author.

Conflicts of Interest: The authors declare no conflicts of interest. The funders had no role in the design of the study; in the collection, analyses, or interpretation of data; in the writing of the manuscript; or in the decision to publish the results.

Abbreviations

The following abbreviations are used in this manuscript:

FBAs	fluorescent base analogues	TCSPC	time-correlated single-photon counting
pC	pyrrolocytosine	CD	circular dichroism
pCr	pC riboside	FDCD	fluorescence-detected CD
2-AP	2-aminopurine	CT	charge transfer
GR	guanine riboswitch	QM	quantum mechanical
G	guanine	ss	single-stranded
Hx	hypoxanthine	ds	double-stranded
WCF	Watson–Crick-Franklin	–	

Appendix A. Selection of Fitting Models for TCSPC

For the complex RNAs reported in this work, we surveyed models containing 2–4 exponential components, as well as gamma (γ) components, which ascribe a decay component to a distribution of closely related structures [62]. We use the notation "xEyG$_{L(S)}$" to concisely indicate a model containing "x" exponential decay components and "y" γ distribution components. L(S) indicates that the γ distribution's mean is longer (shorter) than the exponential component's time constant. An ideal fitting model will have a reduced χ^2 value close to 1 and have unstructured residuals. χ^2 values below 1.3 are generally considered acceptable, though values below 1.2 were obtainable for all pC-containing model oligonucleotides previously investigated by our lab [34]. For the data reported here, however, χ^2 values of 1.2–1.3 were often observed across a range of models of varying complexity. For

example, the single-stranded 21-mer St1ApCA exhibited an average χ^2 of 1.27 when fitted with a 2E model, which improved only marginally to 1.25–1.26 across a wide range of more complex models (Table A1).

Because the χ^2 values were marginal (1.2–1.3) under all tested models in certain cases, we considered the residuals more closely. An ideal model will have residuals that lack autocorrelation and are randomly distributed above and below zero. These properties can be quantified with the Durbin–Watson (DW) parameter and Runs Z test. Residuals are considered uncorrelated at the 95% confidence level if the DW parameter is between 1.75 and 2.25, with a value of 2 indicating no autocorrelation. Residuals are considered random at the 95% confidence level if the Z parameter is between −1.96 and 1.96, with the ideal value being 0 [74].

Below, we compare the χ^2, Durbin–Watson and Z values across six models that were used to fit the decays of St1ApCA at pH 7.4. It is evident that models of complexity beyond 2E yield only small improvements in χ^2, and that all models exhibit acceptable DW and Z values. 2E, 1E1G_S, and 2G models were in agreement about the behavior of this RNA, all showing a short component of population weight ~0.3 and lifetime ~4–5 ns, and a long component of lifetime ~12 ns accounting for the remainder of the population weight. We therefore selected the simple 2E model as representative of this family of behavior.

Table A1. χ^2, Durbin–Watson parameter and Runs Z test value for different models fit to decays of St1ApCA. Values represent average across three successive data accumulations. Green background indicates the model that was selected for this RNA.

Model	χ^2	Durbin–Watson	|Z| [1]
2E	1.27	2.02	1.07
3E	1.25	2.05	0.85
4E	1.25	2.05	0.69
1E1G_L	1.26	2.04	0.95
1E1G_S	1.26	2.04	0.93
2G	1.26	2.03	1.16

[1] Reported Z values represent the average of the absolute value in each replicate.

For the three double-stranded 21-mers investigated here, 1:2UGU, 1:2UIU and 1:2UUU, the 2E fit was notably poor and all other models tested yielded a significant improvement in χ^2. 3E was significantly better than 2E, 1E1G_S or 1E1G_L for 1:2UIU, was somewhat better for 1:2UUU, and was roughly comparable for 1:2UGU. For ease of comparison, we therefore selected 3E models for all double-stranded 21-mers. This contrasts with the previously investigated double-stranded 21-mers, which contained pC between two C residues opposite either GGG (fully complementary) or GUG (mismatched) and were well fit by 2E models (χ^2 = 1.18 and 1.13, respectively) [34].

2E models were universally poor for pC71 and pC74 GR. For pC71 at pH 7.4, we selected a 1E1G_S model, which yielded the best χ^2 value and residual characteristics under the four measurement conditions tested (alone, +Mg^{2+}, +G and +Hx) (values for RNA alone shown in Table A5 as an example).

pC74 also exhibited a significant improvement in χ^2 upon transitioning from a 2E model to a 3E or distribution model. Under 3E, 1E1G_L and 1E1G_S models, χ^2 remained above 1.2 but the DW and Z parameters both suggested that residuals were random (values for RNA alone shown in Table A6 as an example). A 3E model was selected among these as it exhibited a slightly better χ^2 and residual characteristics across the four conditions tested (alone, +Mg^{2+}, +G and +Hx). Only one replicate of pC74 yielded physically reasonable parameter values under a 4E model, and the χ^2 value for that replicate improved only to 1.21 from 1.22 for a 3E fit.

Table A2. χ^2, Durbin–Watson parameter and Runs Z test value for different models fit to decays of 1:2UGU. Values represent average across three successive data accumulations. Green background indicates the model that was selected for this RNA.

Model	χ^2	Durbin–Watson	|Z| [1]
2E	1.74	1.21	12.2
3E	1.12	1.88	1.93
$1E1G_L$	1.13	1.88	1.18
$1E1G_S$	1.15	1.84	2.25
2G	1.10	1.92	1.77

[1] Reported Z values represent the average of the absolute value in each replicate.

Table A3. χ^2, Durbin–Watson parameter and Runs Z test value for different models fit to decays of 1:2UIU. Values represent average across three successive data accumulations. Green background indicates the model that was selected for this RNA.

Model	χ^2	Durbin–Watson	|Z| [1]
2E	1.96	1.26	8.53
3E	1.27	1.91	0.85
$1E1G_L$	1.37	1.79	0.89
$1E1G_S$	1.42	1.74	1.93
2G	1.27	1.92	0.99

[1] Reported Z values represent the average of the absolute value in each replicate.

Table A4. χ^2, Durbin–Watson parameter and Runs Z test value for different models fit to decays of 1:2UUU. Values represent the average across three successive data accumulations. Green background indicates the model that was selected for this RNA.

Model	χ^2	Durbin–Watson	|Z| [1]
2E	1.38	1.63	5.66
3E	1.17	1.91	1.29
$1E1G_L$	1.22	1.85	2.18
$1E1G_S$	1.20	1.88	1.89
2G	1.19	1.89	1.82

[1] Reported Z values represent the average of the absolute value in each replicate.

Table A5. χ^2, Durbin–Watson parameter and Runs Z test value for different models fit to decays of pC71. Values represent the average across three successive data accumulations. Green background indicates the model that was selected for this RNA.

Model	χ^2	Durbin–Watson	|Z| [1]
2E	1.48	1.40	6.90
3E	1.11	1.87	1.55
$1E1G_L$	1.16	1.83	1.49
$1E1G_S$	1.10	1.90	0.90

[1] Reported Z values represent the average of the absolute value in each replicate.

Table A6. χ^2, Durbin–Watson parameter and Runs Z test value for different models fit to decays of pC74. Values represent the average across three successive data accumulations. Green background indicates the model that was selected for this RNA.

Model	χ^2	Durbin–Watson	|Z| [1]
2E	1.35	1.82	2.17
3E	1.21	2.02	0.52
$1E1G_L$	1.23	1.98	0.80
$1E1G_S$	1.23	1.98	0.59

[1] Reported Z values represent the average of the absolute value in each replicate.

References

1. Chauvier, A.; Walter, N.G. Regulation of Bacterial Gene Expression by Non-Coding RNA: It Is All about Time! *Cell Chem. Biol.* **2024**, *31*, 71–85. [CrossRef]
2. Nemeth, K.; Bayraktar, R.; Ferracin, M.; Calin, G.A. Non-Coding RNAs in Disease: From Mechanisms to Therapeutics. *Nat. Rev. Genet.* **2024**, *25*, 211–232. [CrossRef]
3. Panchal, V.; Brenk, R. Riboswitches as Drug Targets for Antibiotics. *Antibiotics* **2021**, *10*, 45. [CrossRef]
4. Ito, M.; Miyata, Y.; Okada, M. Current Clinical Trials with Non-Coding RNA-Based Therapeutics in Malignant Diseases: A Systematic Review. *Transl. Oncol.* **2023**, *31*, 101634. [CrossRef]
5. Stephen, C.; Palmer, D.; Mishanina, T.V. Opportunities for Riboswitch Inhibition by Targeting Co-Transcriptional RNA Folding Events. *Int. J. Mol. Sci.* **2024**, *25*, 10495. [CrossRef]
6. Li, C.; Yang, X.; Dickerson, K.A.; Zanon, P.R.A.; Springer, N.A.; Wang, J.; Jia, Y.; Munshi, N.C.; Batey, R.T.; Disney, M.D. Structure-Guided Design of a Bioactive Covalent Small Molecule Targeting a Riboswitch. *J. Am. Chem. Soc.* **2025**, *147*, 38684–38690. [CrossRef]
7. Mandal, M.; Breaker, R.R. Gene Regulation by Riboswitches. *Nat. Rev. Mol. Cell Biol.* **2004**, *5*, 451–463. [CrossRef]
8. Garst, A.D.; Edwards, A.L.; Batey, R.T. Riboswitches: Structures and Mechanisms. *Cold Spring Harb. Perspect. Biol.* **2011**, *3*, a003533. [CrossRef]
9. Kim, J.N.; Breaker, R.R. Purine Sensing by Riboswitches. *Biol. Cell* **2008**, *100*, 1–11. [CrossRef]
10. Mulhbacher, J.; Brouillette, E.; Allard, M.; Fortier, L.-C.; Malouin, F.; Lafontaine, D.A. Novel Riboswitch Ligand Analogs as Selective Inhibitors of Guanine-Related Metabolic Pathways. *PLoS Pathog.* **2010**, *6*, e1000865. [CrossRef]
11. Ster, C.; Allard, M.; Boulanger, S.; Lamontagne Boulet, M.; Mulhbacher, J.; Lafontaine, D.A.; Marsault, É.; Lacasse, P.; Malouin, F. Experimental Treatment of *Staphylococcus aureus* Bovine Intramammary Infection Using a Guanine Riboswitch Ligand Analog. *J. Dairy Sci.* **2013**, *96*, 1000–1008. [CrossRef]
12. Yan, L.-H.; Le Roux, A.; Boyapelly, K.; Lamontagne, A.-M.; Archambault, M.-A.; Picard-Jean, F.; Lalonde-Seguin, D.; St-Pierre, E.; Najmanovich, R.J.; Fortier, L.-C.; et al. Purine Analogs Targeting the Guanine Riboswitch as Potential Antibiotics against *Clostridioides difficile*. *Eur. J. Med. Chem.* **2018**, *143*, 755–768. [CrossRef]
13. Jain, S.S.; McLaughlin, E.C.; Perron, G.G.; Uppuladinne, M.; Kim, S.; Gindinova, K.; Lundgren, S.H.; Elmelech, L.; Sonavane, U.; Joshi, R.; et al. Inhibition of Xpt Guanine Riboswitch by a Synthetic Nucleoside Analog. *PLoS ONE* **2025**, *20*, e0322308. [CrossRef]
14. Savinov, A.; Perez, C.F.; Block, S.M. Single-Molecule Studies of Riboswitch Folding. *Biochim. Biophys. Acta BBA-Gene Regul. Mech.* **2014**, *1839*, 1030–1045. [CrossRef]
15. Ray, S.; Wdom, J.R.; Walter, N.G. Life under the Microscope: Single-Molecule Fluorescence Highlights the RNA World. *Chem. Rev.* **2018**, *118*, 4120–4155. [CrossRef]
16. McGovern-Gooch, K.R.; Baird, N.J. Fluorescence-Based Investigations of RNA-Small Molecule Interactions. *Methods* **2019**, *167*, 54–65. [CrossRef]
17. Widom, J.R.; Hoeher, J.E. Base-Stacking Heterogeneity in RNA Resolved by Fluorescence-Detected Circular Dichroism Spectroscopy. *J. Phys. Chem. Lett.* **2022**, *13*, 8010–8018. [CrossRef]
18. Shin, D.; Sinkeldam, R.W.; Tor, Y. Emissive RNA Alphabet. *J. Am. Chem. Soc.* **2011**, *133*, 14912–14915. [CrossRef]
19. Tor, Y. Isomorphic Fluorescent Nucleosides. *Acc. Chem. Res.* **2024**, *57*, 1325–1335. [CrossRef]
20. Hoeher, J.E.; Sande, N.E.; Widom, J.R. Probing and Perturbing Riboswitch Folding Using a Fluorescent Base Analogue. *Photochem. Photobiol.* **2024**, *100*, 419–433. [CrossRef]
21. Burns, D.D.; Teppang, K.L.; Lee, R.W.; Lokensgard, M.E.; Purse, B.W. Fluorescence Turn-On Sensing of DNA Duplex Formation by a Tricyclic Cytidine Analogue. *J. Am. Chem. Soc.* **2017**, *139*, 1372–1375. [CrossRef]
22. Ballin, J.D.; Prevas, J.P.; Bharill, S.; Gryczynski, I.; Gryczynski, Z.; Wilson, G.M. Local RNA Conformational Dynamics Revealed by 2-Aminopurine Solvent Accessibility. *Biochemistry* **2008**, *47*, 7043–7052. [CrossRef]
23. Ji, H.; Johnson, N.P.; Von Hippel, P.H.; Marcus, A.H. Local DNA Base Conformations and Ligand Intercalation in DNA Constructs Containing Optical Probes. *Biophys. J.* **2019**, *117*, 1101–1115. [CrossRef]
24. Grytsyk, N.; Richert, L.; Didier, P.; Dziuba, D.; Ciaco, S.; Mazzoleni, V.; Lequeu, T.; Mori, M.; Tor, Y.; Martinez-Fernandez, L.; et al. Thienoguanosine, a Unique Non-Perturbing Reporter for Investigating Rotational Dynamics of DNA Duplexes and Their Complexes with Proteins. *Int. J. Biol. Macromol.* **2022**, *213*, 210–225. [CrossRef]
25. Le, H.-N.; Kuchlyan, J.; Baladi, T.; Albinsson, B.; Dahlén, A.; Wilhelmsson, L.M. Synthesis and Photophysical Characterization of a pH-Sensitive Quadracyclic Uridine (qU) Analogue. *Chem.-Eur. J.* **2024**, *30*, e202303539. [CrossRef]
26. Karlsson, A.F.E.; Pfeiffer, P.; Le, H.-N.; Baladi, T.; Dahlén, A.; Wilhelmsson, L.M. Increased Brightness of Fluorescent Uridine, qU, inside Single- and Double-Stranded RNA. *Sci. Rep.* **2026**, *16*, 8481. [CrossRef]
27. Li, D.; Zhuang, B.; Song, Z.; Gai, F. Development of Indole-Based Hydration-Sensitive Fluorescent Nucleoside Analogues: Experimental and Computational Studies. *Phys. Chem. Chem. Phys.* **2026**, *28*, 17105–17113. [CrossRef]
28. Sansom, H.G.; Bailie, A.E.; Stefanou, F.; Purse, B.W.; Jones, A.C.; Magennis, S.W. Two-Photon Excitation Enables Single-Molecule Detection of a Fluorescent Base Analogue in DNA with High Photostability. *Chem. Sci.* **2026**, *17*, 4174–4182. [CrossRef]

29. Liu, C.; Martin, C.T. Fluorescence Characterization of the Transcription Bubble in Elongation Complexes of T7 RNA polymerase. *J. Mol. Biol.* **2001**, *308*, 465–475. [CrossRef]
30. Buskiewicz, I.A.; Burke, J.M. Folding of the Hammerhead Ribozyme: Pyrrolo-Cytosine Fluorescence Separates Core Folding from Global Folding and Reveals a pH-Dependent Conformational Change. *RNA* **2012**, *18*, 434–448. [CrossRef]
31. Zhang, J.; Ferré-D'Amaré, A.R. Direct Evaluation of tRNA Aminoacylation Status by the T-Box Riboswitch Using tRNA-mRNA Stacking and Steric Readout. *Mol. Cell* **2014**, *55*, 148–155. [CrossRef]
32. Hardman, S.J.O.; Thompson, K.C. Influence of Base Stacking and Hydrogen Bonding on the Fluorescence of 2-Aminopurine and Pyrrolocytosine in Nucleic Acids. *Biochemistry* **2006**, *45*, 9145–9155. [CrossRef]
33. Hardman, S.J.O.; Botchway, S.W.; Thompson, K.C. Evidence for a Nonbase Stacking Effect for the Environment-Sensitive Fluorescent Base Pyrrolocytosine—Comparison with 2-Aminopurine. *Photochem. Photobiol.* **2008**, *84*, 1473–1479. [CrossRef]
34. Coulson, T.L.; Widom, J.R. Impacts of Sequence and Structure on Pyrrolocytosine Fluorescence in RNA. *Nucleic Acids Res.* **2025**, *53*, gkaf262. [CrossRef]
35. Roca, J.; Hori, N.; Baral, S.; Velmurugu, Y.; Narayanan, R.; Narayanan, P.; Thirumalai, D.; Ansari, A. Monovalent Ions Modulate the Flux through Multiple Folding Pathways of an RNA Pseudoknot. *Proc. Natl. Acad. Sci. USA* **2018**, *115*, E7313–E7322. [CrossRef]
36. Lang, K.; Rieder, R.; Micura, R. Ligand-Induced Folding of the thiM TPP Riboswitch Investigated by a Structure-Based Fluorescence Spectroscopic Approach. *Nucleic Acids Res.* **2007**, *35*, 5370–5378. [CrossRef]
37. Serganov, A.; Polonskaia, A.; Phan, A.T.; Breaker, R.R.; Patel, D.J. Structural Basis for Gene Regulation by a Thiamine Pyrophosphate-Sensing Riboswitch. *Nature* **2006**, *441*, 1167–1171. [CrossRef]
38. Heppell, B.; Lafontaine, D.A. Folding of the SAM Aptamer Is Determined by the Formation of a K-Turn-Dependent Pseudoknot. *Biochemistry* **2008**, *47*, 1490–1499. [CrossRef]
39. Petrone, P.M.; Dewhurst, J.; Tommasi, R.; Whitehead, L.; Pomerantz, A.K. Atomic-Scale Characterization of Conformational Changes in the preQ1 Riboswitch Aptamer upon Ligand Binding. *J. Mol. Graph. Model.* **2011**, *30*, 179–185. [CrossRef]
40. Wickiser, J.K.; Cheah, M.T.; Breaker, R.R.; Crothers, D.M. The Kinetics of Ligand Binding by an Adenine-Sensing Riboswitch. *Biochemistry* **2005**, *44*, 13404–13414. [CrossRef]
41. Gilbert, S.D.; Stoddard, C.D.; Wise, S.J.; Batey, R.T. Thermodynamic and Kinetic Characterization of Ligand Binding to the Purine Riboswitch Aptamer Domain. *J. Mol. Biol.* **2006**, *359*, 754–768. Erratum in *J. Mol. Biol.* **2006**, *363*, 624. [CrossRef]
42. Mulhbacher, J.; Lafontaine, D.A. Ligand Recognition Determinants of Guanine Riboswitches. *Nucleic Acids Res.* **2007**, *35*, 5568–5580. [CrossRef]
43. Jean, J.M.; Hall, K.B. 2-Aminopurine Fluorescence Quenching and Lifetimes: Role of Base Stacking. *Proc. Natl. Acad. Sci. USA* **2001**, *98*, 37–41. [CrossRef]
44. Kodali, G.; Narayanan, M.; Stanley, R.J. Excited-State Electronic Properties of 6-Methylisoxanthopterin (6-MI): An Experimental and Theoretical Study. *J. Phys. Chem. B* **2012**, *116*, 2981–2989. [CrossRef]
45. Batey, R.T.; Gilbert, S.D.; Montange, R.K. Structure of a Natural Guanine-Responsive Riboswitch Complexed with the Metabolite Hypoxanthine. *Nature* **2004**, *432*, 411–415. [CrossRef]
46. Buck, J.; Noeske, J.; Wöhnert, J.; Schwalbe, H. Dissecting the Influence of Mg2+ on 3D Architecture and Ligand-Binding of the Guanine-Sensing Riboswitch Aptamer Domain. *Nucleic Acids Res.* **2010**, *38*, 4143–4153. [CrossRef]
47. Buck, J.; Wacker, A.; Warkentin, E.; Wöhnert, J.; Wirmer-Bartoschek, J.; Schwalbe, H. Influence of Ground-State Structure and Mg 2+ Binding on Folding Kinetics of the Guanine-Sensing Riboswitch Aptamer Domain. *Nucleic Acids Res.* **2011**, *39*, 9768–9778. [CrossRef]
48. Mandal, M.; Breaker, R.R. Adenine Riboswitches and Gene Activation by Disruption of a Transcription Terminator. *Nat. Struct. Mol. Biol.* **2004**, *11*, 29–35. [CrossRef]
49. Kim, J.N.; Blount, K.F.; Puskarz, I.; Lim, J.; Link, K.H.; Breaker, R.R. Design and Antimicrobial Action of Purine Analogues That Bind Guanine Riboswitches. *ACS Chem. Biol.* **2009**, *4*, 915–927. [CrossRef]
50. Mandal, M.; Boese, B.; Barrick, J.E.; Winkler, W.C.; Breaker, R.R. Riboswitches Control Fundamental Biochemical Pathways in *Bacillus subtilis* and Other Bacteria. *Cell* **2003**, *113*, 577–586. [CrossRef]
51. Serganov, A.; Yuan, Y.-R.; Pikovskaya, O.; Polonskaia, A.; Malinina, L.; Phan, A.T.; Hobartner, C.; Micura, R.; Breaker, R.R.; Patel, D.J. Structural Basis for Discriminative Regulation of Gene Expression by Adenine- and Guanine-Sensing mRNAs. *Chem. Biol.* **2004**, *11*, 1729–1741. [CrossRef]
52. Noeske, J.; Buck, J.; Fürtig, B.; Nasiri, H.R.; Schwalbe, H.; Wöhnert, J. Interplay of 'Induced Fit' and Preorganization in the Ligand Induced Folding of the Aptamer Domain of the Guanine Binding Riboswitch. *Nucleic Acids Res.* **2007**, *35*, 572–583. [CrossRef]
53. Gilbert, S.D.; Love, C.E.; Edwards, A.L.; Batey, R.T. Mutational Analysis of the Purine Riboswitch Aptamer Domain. *Biochemistry* **2007**, *46*, 13297–13309. [CrossRef]
54. Brenner, M.D.; Scanlan, M.S.; Nahas, M.K.; Ha, T.; Silverman, S.K. Multivector Fluorescence Analysis of the Xpt Guanine Riboswitch Aptamer Domain and the Conformational Role of Guanine. *Biochemistry* **2010**, *49*, 1596–1605. Erratum in *Biochemistry*. **2010**, *49*, 2306. [CrossRef]

55. Hamal Dhakal, S.; Panchapakesan, S.S.S.; Slattery, P.; Roth, A.; Breaker, R.R. Variants of the Guanine Riboswitch Class Exhibit Altered Ligand Specificities for Xanthine, Guanine, or 2′-Deoxyguanosine. *Proc. Natl. Acad. Sci. USA* **2022**, *119*, e2120246119. [CrossRef]
56. Gilbert, S.D.; Reyes, F.E.; Edwards, A.L.; Batey, R.T. Adaptive Ligand Binding by the Purine Riboswitch in the Recognition of Guanine and Adenine Analogs. *Structure* **2009**, *17*, 857–868. [CrossRef]
57. O'Neil, M.A.; Barton, J.K. 2-Aminopurine: A Probe of Structural Dynamics and Charge Transfer in DNA and DNA:RNA Hybrids. *J. Am. Chem. Soc.* **2002**, *124*, 13053–13066. [CrossRef]
58. Wan, C.; Fiebig, T.; Schiemann, O.; Barton, J.K.; Zewail, A.H. Femtosecond Direct Observation of Charge Transfer between Bases in DNA. *Proc. Natl. Acad. Sci. USA* **2000**, *97*, 14052–14055. [CrossRef]
59. Kenfack, C.A.; Burger, A.; Mély, Y. Excited-State Properties and Transitions of Fluorescent 8-Vinyl Adenosine in DNA. *J. Phys. Chem. B* **2006**, *110*, 26327–26336. [CrossRef]
60. Kuchlyan, J.; Martinez-Fernandez, L.; Mori, M.; Gavvala, K.; Ciaco, S.; Boudier, C.; Richert, L.; Didier, P.; Tor, Y.; Improta, R.; et al. What Makes Thienoguanosine an Outstanding Fluorescent DNA Probe? *J. Am. Chem. Soc.* **2020**, *142*, 16999–17014. [CrossRef]
61. Zhang, L.; Zhang, Y. Theoretical Insights Into the Photophysical Properties of the Isomorphic Fluorescent RNA Alphabet Derived From the Trifluoromethylthieno [3,4-d]Pyrimidine Core. *Int. J. Quantum Chem.* **2026**, *126*, e70163. [CrossRef]
62. Fogarty, A.C.; Jones, A.C.; Camp, P.J. Extraction of Lifetime Distributions from Fluorescence Decays with Application to DNA-Base Analogues. *Phys. Chem. Chem. Phys.* **2011**, *13*, 3819–3830. [CrossRef]
63. Cavaluzzi, M.J.; Borer, P.N. Revised UV Extinction Coefficients for Nucleoside-5′-Monophosphates and Unpaired DNA and RNA. *Nucleic Acids Res.* **2004**, *32*, e13. [CrossRef]
64. Nomanbhoy, T.K.; Cerione, R. Characterization of the Interaction between RhoGDI and Cdc42Hs Using Fluorescence Spectroscopy. *J. Biol. Chem.* **1996**, *271*, 10004–10009. [CrossRef]
65. Nagel, J.H.A.; Gultyaev, A.P.; Öistämö, K.J.; Gerdes, K.; Pleij, C.W.A. A pH-Jump Approach for Investigating Secondary Structure Refolding Kinetics in RNA. *Nucleic Acids Res.* **2002**, *30*, e63. [CrossRef]
66. Cuniasse, P.; Fazakerley, G.V.; Guschlbauer, W.; Kaplan, B.E.; Sowers, L.C. The Abasic Site as a Challenge to DNA Polymerase: A Nuclear Magnetic Resonance Study of G, C and T Opposite a Model Abasic Site. *J. Mol. Biol.* **1990**, *213*, 303–314. [CrossRef]
67. Guest, C.R.; Hochstrasser, R.A.; Sowers, L.C.; Millar, D.P. Dynamics of Mismatched Base Pairs in DNA. *Biochemistry* **1991**, *30*, 3271–3279. [CrossRef]
68. Xu, D.; Evans, K.O.; Nordlund, T.M. Melting and Premelting Transitions of an Oligomer Measured by DNA Base Fluorescence and Absorption. *Biochemistry* **1994**, *33*, 9592–9599. [CrossRef]
69. Ratliff, R.L.; Liu, J.-J.; Vaughan, M.R.; Gray, D.M. Sequence-Dependence of the CD of Synthetic Double-Stranded RNAs Containing Inosinate Instead of Guanylate Subunits. *Biopolymers* **1986**, *25*, 1735–1750. [CrossRef]
70. Chauca-Diaz, A.M.; Jung Choi, Y.; Resendiz, M.J.E. Biophysical Properties and Thermal Stability of Oligonucleotides of RNA Containing 7,8-Dihydro-8-Hydroxyadenosine. *Biopolymers* **2015**, *103*, 167–174. [CrossRef]
71. Miyahara, T.; Nakatsuji, H.; Sugiyama, H. Similarities and Differences between RNA and DNA Double-Helical Structures in Circular Dichroism Spectroscopy: A SAC–CI Study. *J. Phys. Chem. A* **2016**, *120*, 9008–9018. [CrossRef]
72. Johnson, N.P.; Baase, W.A.; von Hippel, P.H. Investigating Local Conformations of Double-Stranded DNA by Low-Energy Circular Dichroism of Pyrrolo-Cytosine. *Proc. Natl. Acad. Sci. USA* **2005**, *102*, 7169–7173. [CrossRef]
73. Tinoco, I.; Turner, D.H. Fluorescence Detected Circular Dichroism. Theory. *J. Am. Chem. Soc.* **1976**, *98*, 6453–6456. [CrossRef]
74. Smith, D.A.; McKenzie, G.; Jones, A.C.; Smith, T.A. Analysis of Time-Correlated Single Photon Counting Data: A Comparative Evaluation of Deterministic and Probabilistic Approaches. *Methods Appl. Fluoresc.* **2017**, *5*, 042001. [CrossRef]
75. Widom, J.R.; Coulson, T.L. Analyzing Structural Heterogeneity in RNA Using Fluorescence-Detected Circular Dichroism Spectroscopy. *Methods Mol. Biol.* **2026**, *3004*, 75–87. [CrossRef]
76. Turner, D.H.; Tinoco, I., Jr.; Maestre, M. Fluorescence Detected Circular Dichroism. *J. Am. Chem. Soc.* **1974**, *96*, 4340–4342. [CrossRef]
77. Glen Report 15.13-Pyrrolo-C—A Novel Fluorescent Nucleoside. Available online: https://www.glenresearch.com/reports/gr15-13 (accessed on 17 October 2026).
78. Frisch, M.J.; Trucks, G.W.; Cheeseman, J.R.; Scalmani, G.; Caricato, M.; Hratchian, H.P.; Li, X.; Barone, V.; Bloino, J.; Zheng, G.; et al. *Gaussian 09, Revision E.01*; Gaussian, Inc.: Wallingford, CT, USA, 2016.
79. Nguyen, Q.L.; Spata, V.A.; Matsika, S. Photophysical Properties of Pyrrolocytosine, a Cytosine Fluorescent Base Analogue. *Phys. Chem. Chem. Phys.* **2016**, *18*, 20189–20198. [CrossRef]

Disclaimer/Publisher's Note: The statements, opinions and data contained in all publications are solely those of the individual author(s) and contributor(s) and not of MDPI and/or the editor(s). MDPI and/or the editor(s) disclaim responsibility for any injury to people or property resulting from any ideas, methods, instructions or products referred to in the content.